




## Singular topology of scattering matrices

Cheng Guo <sup>1,\*</sup>, Jiazheng Li <sup>2</sup>, Meng Xiao <sup>2</sup> and Shanhui Fan <sup>3,†</sup><sup>1</sup>*Department of Applied Physics, Stanford University, Stanford, California 94305, USA*<sup>2</sup>*Key Laboratory of Artificial Micro- and Nano-Structures of Ministry of Education and School of Physics and Technology, Wuhan University, Wuhan 430072, China*<sup>3</sup>*Ginzton Laboratory and Department of Electrical Engineering, Stanford University, Stanford, California 94305, USA*

(Received 20 April 2023; revised 28 September 2023; accepted 2 October 2023; published 17 October 2023)

We present a systematic topological theory of the scattering matrix and its submatrices, focusing on the singular values and vectors. We study the topological properties of the scattering matrix in the parameter space and determine a set of topological characteristics for a general system, including the winding number, Berry phase, and skew polarization. We reveal unique topological effects for a reciprocal system such as quantized single-band polarization and  $\mathbb{Z}_2$  topology of Takagi vectors. Applying our theory, we reveal the topological nature of two phenomena: the well-known effect of coherent perfect absorption and a new effect we call coherent perfect extinction. Coherent perfect extinction refers to the complete extinction of light due to interference of multiple incident waves. It accounts for both absorption and scattering losses and encompasses many other known effects such as complete polarization conversion and reflectionless scattering modes, providing a unifying theme for these phenomena. Our analysis highlights the topological nature of these effects and provides criteria to localize their occurrence in parameter space, facilitating optical design to achieve these effects. We propose utilizing coherent perfect extinction for multichannel background-free sensing. These findings significantly advance our understanding of scattering phenomena and have important implications for the development of novel optical devices.

DOI: [10.1103/PhysRevB.108.155418](https://doi.org/10.1103/PhysRevB.108.155418)

## I. INTRODUCTION

Topology is widely used in modern physics and provides a powerful framework for understanding physical phenomena [1–4]. Extensive research has been conducted on the topology of the Hamiltonian in the parameter space such as the Brillouin zone [5,6], leading to significant discoveries such as the TKNN formula [7], Berry phase [8,9], and topological insulators [10–12].

In addition to the Hamiltonian, the scattering matrix ( $S$  matrix) [13] is another crucial characterization of a physical system. The scattering matrix is directly measurable and essential in understanding physical phenomena such as electron transport [14], light scattering [15,16], and particle collisions [17]. It is therefore useful to study the topology of scattering matrices. The topology of a single scattering matrix element has been discussed in various contexts, including optical vortices [18–24], polarization conversion [25–30], optical computation [31,32], exceptional points [33,34], and scattering anomalies [35,36]. However, there has been only limited discussion regarding the topology of the entire scattering matrix and its submatrices [37–40].

In this paper, we study the topology of scattering matrices, focusing on the singular values and vectors [41]. Singular values and vectors are fundamental characteristics of a scattering matrix and have direct implications on basic phenomena including transmission [42], reflection [43], absorption, and

emission [44,45]. They are also essential in applications such as imaging [46,47], integrated photonics [48,49], and optical neural networks [50].

Our main results are as follows. Firstly, we develop a general theory on the singular topology of scattering matrices. We analyze the evolution of a scattering matrix along a loop in the parameter space and determine a set of topological characteristics, including the winding number, Berry phase, and skew polarization. We further reveal the unique topological effects of a reciprocal system, such as quantized single-band polarization and  $\mathbb{Z}_2$  topology of Takagi vectors. Then, we apply our general theory to reveal the topological nature of two phenomena: the well-known effect of coherent perfect absorption [51] and a new effect we call coherent perfect extinction.

Coherent perfect absorption refers to the complete absorption of light due to the interference of multiple incident waves [51]. While this effect has been extensively studied [22,51–59], its topological nature has not been recognized beyond the one-port case (i.e., the case of critical coupling [15]). Coherent perfect extinction refers to the complete extinction of light due to interference of multiple incident waves. This effect generalizes the notion of coherent perfect absorption, and differs in that it accounts for both absorption and scattering losses. Additionally, coherent perfect extinction encompasses other physical effects such as complete polarization conversion [25] and reflectionless scattering modes [60–62]. Our theory points to topological concepts as a unifying theme that underlies these seemingly disparate phenomena. Our analysis highlights the topological robustness of these effects under generic parameter perturbations and provides criteria to localize their occurrence in parameter space, facilitating optical

\*guocheng@stanford.edu

†shanhui@stanford.edu

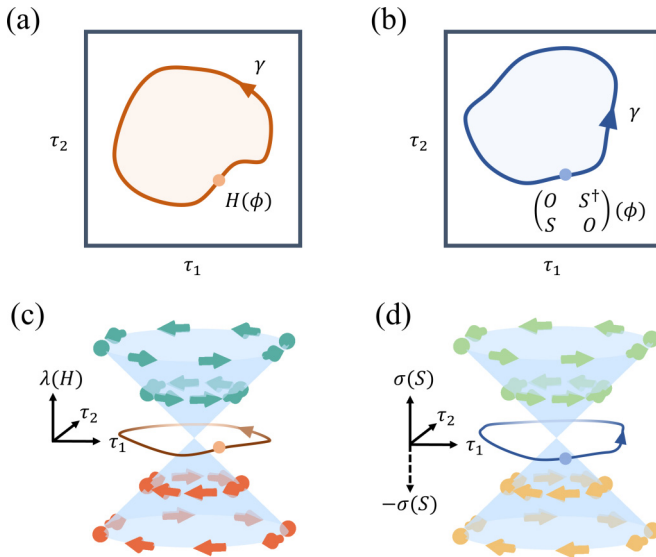


FIG. 1. Eigen topology of a Hermitian matrix  $H$  vs singular topology of a scattering matrix  $S$ . (a)  $H$  depends on parameters  $(\tau_1, \tau_2)$ , where  $\gamma$  is a loop in the parameter space. Here the parameter space is two-dimensional, but in general, it can have an arbitrary dimension. (b)  $S$  depends on  $(\tau_1, \tau_2)$ . From  $S$  we construct a Hermitian block matrix. (c) Eigen topology of  $H$ . We showcase a Dirac cone with sheets representing eigenvalues and arrows representing eigenvectors as Bloch vectors. (d) Singular topology of  $S$  is connected to eigentopology of the block matrix. We showcase the effective two-band model of coherent perfect absorption. The sheets represent the eigenvalues of the block matrix, which equals the singular values of  $S$  and their negation. The arrows represent the eigenvectors of the block matrix, which are related to the left and right singular vectors of  $S$ .

design to achieve these effects. As a practical application, we propose utilizing coherent perfect extinction for multi-channel background-free sensing. These findings significantly advance our understanding of various scattering phenomena and have important implications for the development of novel optical devices.

Our work reveals a fundamental connection between the singular topology of a scattering matrix  $S$  and the eigentopology of a chiral symmetric Hermitian matrix

$$H = \begin{pmatrix} 0 & S^\dagger \\ S & 0 \end{pmatrix}. \quad (1)$$

[See Figs. 1(a) and 1(b).] While this block matrix technique has been previously utilized in the study of Floquet operators [63] and non-Hermitian Hamiltonians [64–67], it has not been applied to the analysis of scattering matrices. By leveraging the well-established techniques of eigentopology of Hermitian matrices, we can systematically study the singular topology of scattering matrices. Our analysis reveals the emergence of similar mathematical patterns in different physics contexts: scattering phenomena and band topology. For instance, we demonstrate that coherent perfect absorption has a mathematical structure isomorphic to the Dirac cone in graphene [see Figs. 1(c) and 1(d)]. We anticipate that further exploration of this correspondence will uncover new topological effects in wave scattering. This approach may also point to new insights

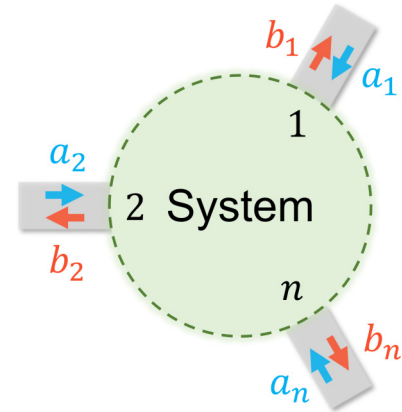


FIG. 2. Scheme of the system.

into other scattering anomalies, including laser anomalies, exceptional points, bound states in the continuum, etc.

This paper primarily focuses on the scattering matrices of bosonic systems, including photonic and acoustic systems. However, with additional caution, many of our findings can also be extended to fermionic systems, such as electronic systems.

The rest of this paper is organized as follows. In Sec. II, we review the scattering matrix and its singular value decomposition. In Sec. III, we develop a general theory on the singular topology of scattering matrices. In Sec. IV, we reveal the topology of coherent perfect absorption. In Sec. V A, we propose coherent perfect extinction and study its topology. We discuss in Sec. VI and conclude in Sec. VII. We introduce mathematical notations as necessary throughout the text. Appendix A provides a comprehensive list of the notations. Appendices B–F provide detailed mathematical proof and conventions.

## II. SCATTERING MATRIX & SINGULAR VALUE DECOMPOSITION

In this section, we briefly review the scattering matrix of a linear system and its singular value decomposition. We elucidate the physical significance of singular values and vectors. We introduce a useful mathematical technique for studying singular value decomposition.

### A. Scattering matrix

A scattering matrix characterizes a system's response to an incoming wave or particle [13]. Consider a general  $n$ -port linear time-invariant system (Fig. 2). Each port is made of lossless reciprocal media and supports an input mode and an output mode, which are time-reversal pairs [15]. Using these modes as orthonormal bases, we describe the incoming and outgoing waves by

$$\mathbf{a} = (a_1, \dots, a_n)^T, \quad \mathbf{b} = (b_1, \dots, b_n)^T, \quad (2)$$

where  $a_i$  and  $b_i$  are the input and output complex amplitudes in the  $i$ th port, respectively. The system is described by a scattering matrix  $S \in M_n$ :

$$\mathbf{b} = S\mathbf{a}, \quad (3)$$

where  $M_n$  denotes the set of  $n \times n$  complex matrices. The matrix element  $S_{ij}$  is the transport coefficient from the  $j$ th to the  $i$ th port; the diagonal and off-diagonal elements are the reflection and transmission coefficients, respectively.

### B. Singular value decomposition

A scattering matrix  $S \in M_n$  is in general complex and is not necessarily Hermitian. Any complex matrix takes singular value decomposition [41]:

$$S = U \Sigma V^\dagger, \quad (4)$$

where  $U, V \in U(n)$  with  $U(n)$  the set of  $n \times n$  unitary matrices, and

$$\Sigma = \text{diag}(\sigma_1, \dots, \sigma_n). \quad (5)$$

Here  $\sigma_1 \geq \dots \geq \sigma_n \geq 0$  are the singular values; the columns of  $U, u_1, \dots, u_n$ , are the left singular vectors; the columns of  $V, v_1, \dots, v_n$ , are the right singular vectors. In terms of these singular values and vectors, Eq. (4) can be rewritten as

$$S = \sum_{i=1}^n \sigma_i u_i v_i^\dagger. \quad (6)$$

The singular values and vectors of the  $S$  matrix are crucial characteristics of a linear system. The  $S$  matrix represents a linear operator that maps from the input space to the output space of waves. The right singular vectors  $\{v_i\}$  and left singular vectors  $\{u_i\}$  form orthonormal bases for the input and output spaces, respectively. The linear system converts a right singular vector  $v_i$  into a left singular vector  $u_i$  with an amplitude given by the singular value  $\sigma_i$  [Eq. (6)]. Thus the left and right singular vectors form mode-converter pairs, while the singular value characterizes the strength of each mode-conversion channel [42,44,68]. These quantities have direct physical significance and impose fundamental bounds on basic phenomena such as transmission [42], reflection [43], absorption, and emission [44,45]. The physical significance of singular values and vectors motivates us to study their topology.

### C. Block matrix technique

Here we review a standard mathematical technique that translates the singular value analysis of a complex matrix (like the  $S$  matrix) into the eigenvalue analysis of a Hermitian matrix [69,70]. This technique has been used in recent studies of topological phases of non-Hermitian systems [64–67,71]. Consider a  $2 \times 2$  block matrix

$$H := \begin{pmatrix} O & S^\dagger \\ S & O \end{pmatrix}, \quad (7)$$

where  $O$  denotes the  $n \times n$  zero matrix. By construction,  $H \in M_{2n}$  is Hermitian and has built-in chiral symmetry [72,73], i.e., there exists a unitary Hermitian matrix  $\Gamma$  such that

$$\Gamma H \Gamma = -H. \quad (8)$$

Here  $\Gamma$  is the block Pauli matrix

$$\Gamma = \Sigma_z = \begin{pmatrix} I & O \\ O & -I \end{pmatrix}, \quad (9)$$

where  $I$  denotes the  $n \times n$  identity matrix.

Now we calculate the eigenvalues and eigenvectors of  $H$ . Let  $\lambda_j$  with  $j = \pm 1, \dots, \pm n$  be the eigenvalues of  $H$  ordered as

$$\lambda_1 \geq \dots \geq \lambda_n \geq \lambda_{-n} \geq \dots \geq \lambda_{-1}, \quad (10)$$

and let  $|\psi_j\rangle$  be the corresponding eigenvectors. Substituting Eq. (4) into Eq. (7), we obtain

$$H = \begin{pmatrix} O & V \Sigma U^\dagger \\ U \Sigma V^\dagger & O \end{pmatrix} = \begin{pmatrix} V & O \\ O & U \end{pmatrix} \begin{pmatrix} O & \Sigma \\ \Sigma & O \end{pmatrix} \begin{pmatrix} V^\dagger & O \\ O & U^\dagger \end{pmatrix}. \quad (11)$$

Therefore the eigenvalues of  $H$  are

$$\lambda_i = \sigma_i, \quad \lambda_{-i} = -\sigma_i, \quad i = 1, \dots, n. \quad (12)$$

The corresponding eigenvectors are

$$|\psi_i\rangle = \frac{1}{\sqrt{2}} e^{i\alpha_i} \begin{pmatrix} v_i \\ u_i \end{pmatrix}, \quad |\psi_{-i}\rangle = \frac{1}{\sqrt{2}} e^{i\alpha_{-i}} \begin{pmatrix} v_i \\ -u_i \end{pmatrix}, \quad (13)$$

where  $\alpha_i$  and  $\alpha_{-i}$  are arbitrary phases.

Equations (12) and (13) relate the singular values and vectors of  $S$  to the eigenvalues and vectors of  $H$ . Moreover, they reveal the relations

$$\lambda_{-i} = -\lambda_i, \quad |\psi_{-i}\rangle = e^{i\delta_i} \Gamma |\psi_i\rangle, \quad (14)$$

where  $\delta_i = \alpha_{-i} - \alpha_i$  is an arbitrary phase. These relations are direct consequences of the chiral symmetry [Eq. (8)] [72,73].

The block matrix technique establishes a direct correspondence between a general scattering matrix  $S \in M_n$  and a chiral symmetric Hermitian matrix  $H$ . The topology of Hermitian matrices has been well studied [74]. For example, there is a complete topological classification of fully gapped Hermitian matrices in terms of time-reversal symmetry, particle-hole symmetry, and chiral symmetry [72]. These known results are useful in studying the topology of scattering matrices.

## III. SINGULAR TOPOLOGY OF SCATTERING MATRICES

In this section, we investigate the singular-value and singular-vector topology of scattering matrices. We first study general systems, then examine reciprocal systems. Here in the study of “general systems,” we do not assume any symmetry, while in the study of “reciprocal systems,” we consider systems that adhere to reciprocity relations, such as photonic systems satisfying Lorentz reciprocity [15] and acoustic systems satisfying Rayleigh reciprocity [75].

### A. General systems

We consider a system described by an  $n \times n$  scattering matrix that depends on some parameters  $\tau \in \Omega$ , where the parameter space  $\Omega$  is a  $p$ -dimensional smooth manifold<sup>1</sup>. For

<sup>1</sup>We recall that a manifold is locally Euclidean: every point  $\tau_c$  in  $\Omega$  has a neighborhood  $U$ , called a chart, that is homeomorphic to an open subset of  $\mathbb{R}^p$ . The homeomorphism defines a coordinate map on  $U: \tau \mapsto (\tau_1, \dots, \tau_p)$ . The coordinates on a chart allow one to carry out computations as though in Euclidean space. Different charts are connected by smooth transition functions. See Ref. [111] for more details about smooth manifolds.

example,  $\Omega$  can be  $\mathbb{R}^p$ , a  $p$ -sphere, or a  $p$ -torus. The system is characterized by the map:

$$S : \Omega \rightarrow M_n \quad \tau \mapsto S(\tau). \quad (15)$$

We assume that  $S$  is continuous. We study the topological properties of  $S$ .

We take a similar approach as Berry's [8]. Consider a closed path or a loop  $\gamma$ :

$$\begin{aligned} \gamma : [0, 2\pi] &\rightarrow \Omega \\ \phi &\mapsto \gamma(\phi), \quad \text{with } \gamma(0) = \gamma(2\pi). \end{aligned} \quad (16)$$

We analyze the cyclic evolution of  $S$  along the loop  $\gamma$  and determine a set of topological quantities that characterizes the homotopy of the composite map:

$$\begin{aligned} S \circ \gamma : [0, 2\pi] &\rightarrow M_n, \\ \phi &\mapsto S(\gamma(\phi)), \quad \text{with } S(\gamma(0)) = S(\gamma(2\pi)). \end{aligned} \quad (17)$$

We assume that  $S \circ \gamma$  is piecewise continuously differentiable and everywhere invertible:

$$\det S(\gamma(\phi)) \neq 0, \quad \forall \phi \in [0, 2\pi]. \quad (18)$$

Condition (18) is generically met since for  $A \in M_n$ ,  $\det A = 0$  is a codimension 2 phenomenon. Typically, achieving  $\det A = 0$  requires adjusting two real parameters, as both the real and imaginary parts of  $\det A$  must vanish. Thus, in a  $p$ -dimensional parameter space, the equation  $\det A = 0$  defines a submanifold of dimension  $(p - 2)$ . A loop like  $\gamma$  as a one-dimensional manifold generically does not intersect with this submanifold, since  $(p - 2) + 1 < p$ . Therefore generically we can assume that the matrix  $S(\gamma(\phi))$  has full rank along the loop  $\gamma$ . Similar codimension arguments will be used throughout this paper.

### 1. Winding number

First, we can calculate the winding number of  $S$  around the loop  $\gamma$ :

$$\text{wind}(S) := \frac{1}{2\pi i} \int_0^{2\pi} \text{Tr} \left( S^{-1} \frac{dS}{d\phi} \right) d\phi, \quad (19)$$

which can be proven to be equal to the winding number of  $\det S$  [76]:

$$\text{wind}(S) = \text{wind}(\det S) := \frac{1}{2\pi i} \int_0^{2\pi} \frac{1}{\det S} \frac{d \det S}{d\phi} d\phi. \quad (20)$$

See Appendix C for proof of Eq. (20). The winding number of  $S$  is an integer:

$$\text{wind}(S) \in \mathbb{Z}. \quad (21)$$

It labels the first homotopy class of  $S$  in the general linear group  $GL(n, \mathbb{C})$  whose fundamental group [77]

$$\pi_1(GL(n, \mathbb{C})) \cong \mathbb{Z}, \quad (22)$$

where  $\cong$  denotes isomorphism. See Appendix B for proof of Eq. (22).

### 2. Berry phase and skew polarization

We can also calculate geometric phases for the singular vectors of  $S$  around  $\gamma$ . We need to further assume that  $S(\gamma(\phi))$  has distinct singular values, i.e.,

$$\sigma_1(\phi) > \sigma_2(\phi) > \dots > \sigma_n(\phi) > 0, \quad \forall \phi \in [0, 2\pi], \quad (23)$$

where  $\sigma_i(\phi)$  denote the  $i$ th singular value of  $S(\gamma(\phi))$ . Since  $S \circ \gamma$  is continuous,  $\sigma_i$  is also continuous. We refer to  $\sigma_i$  as the  $i$ th *singular band* (of  $S$ ). In condition (23),  $\sigma_n(\phi) > 0$  is equivalent to condition (18), while the other inequalities require all the singular bands to be fully gapped. The latter is generically met since for  $S \in M_n$ , having two equal singular values is a codimension 3 phenomenon [78]. If condition (23) is not met, one can either apply a small generic perturbation to restore condition (23), or treat a group of bands glued together by degeneracies as a whole and develop a multiband formulation [6]. We will assume that condition (23) is true for simplicity.

We apply the block matrix technique as discussed in Sec. II C. From  $S(\gamma(\phi))$ , we construct  $H(\gamma(\phi))$  by Eq. (7) and calculate its eigenvalues  $\lambda_j(\phi)$  and eigenvectors  $|\psi_j(\phi)\rangle$  with  $j = \pm 1, \dots, \pm n$ . From Eq. (12) and condition (23),

$$\begin{aligned} \lambda_1(\phi) &> \dots > \lambda_n(\phi) > 0 > \lambda_{-n}(\phi) > \dots > \lambda_{-1}(\phi), \\ \forall \phi &\in [0, 2\pi]. \end{aligned} \quad (24)$$

Since  $\lambda_{\pm i}(\phi) = \pm \sigma_i(\phi)$  and  $\sigma_i$  is continuous,  $\lambda_j$  is also continuous. We refer to  $\lambda_j$  as the  $j$ th *eigenband* (of  $H$ ). Condition 24 indicates that all the eigenbands are fully gapped. Consequently, each eigenvector  $|\psi_j(\phi)\rangle$  possesses well-defined geometric phases around  $\gamma$ . Since  $H(\gamma(\phi))$  has built-in chiral symmetry, there are two different geometric phases: polarization (Berry phase) and skew polarization [79].

First, we calculate the polarization of each eigenband [6]:

$$P_j := \frac{1}{2\pi} \int_0^{2\pi} A_j(\phi) d\phi, \quad A_j(\phi) = i \langle \psi_j(\phi) | \partial_\phi | \psi_j(\phi) \rangle, \quad (25)$$

which is the Berry phase of  $|\psi_j(\phi)\rangle$  around  $\gamma$  in units of  $2\pi$  [8,9]. We note that  $P_j$  is well defined only modulo 1 [6]. Consider a gauge transformation

$$|\psi'_j(\phi)\rangle = e^{-i\beta(\phi)} |\psi_j(\phi)\rangle, \quad (26)$$

where  $\beta(\phi)$  is a continuous real function with

$$\beta(2\pi) = \beta(0) + 2\pi k, \quad k \in \mathbb{Z}. \quad (27)$$

Then Eq. (25) is transformed according to

$$A'_j(\phi) = A_j(\phi) + \frac{d\beta(\phi)}{d\phi}, \quad P'_j = P_j + k, \quad (28)$$

thus  $P_j$  is gauge-invariant only modulo 1. The chiral symmetry relates  $P_i$  and  $P_{-i}$ . Substituting Eq. (13) into Eq. (25), we obtain

$$A_{-i}(\phi) = A_i(\phi), \quad P_{-i} = P_i. \quad (29)$$

One can further prove that the total polarization of all the positive (or negative) eigenbands

$$P := \sum_{i=1}^n P_i = \sum_{i=1}^n P_{-i} \quad (30)$$

can only take the values 0 and  $\frac{1}{2}$  modulo 1 [79,80]:

$$P \equiv 0, \quad \text{or} \quad P \equiv \frac{1}{2}. \quad (31)$$

Throughout the paper,  $\equiv$  denotes congruence modulo 1 (mod 1) [81].

Second, we calculate the skew polarization of each eigenband [79,82]:

$$v_j := \frac{1}{\pi} \int_0^{2\pi} \tilde{A}(\phi) d\phi, \quad \tilde{A}(\phi) = i \langle \Gamma \psi_j(\phi) | \partial_\phi | \psi_j(\phi) \rangle, \quad (32)$$

which is well-defined for fully gapped chiral symmetric systems. We note that  $v_j$  is invariant under the gauge transformation in Eq. (26). The chiral symmetry relates  $v_i$  and  $v_{-i}$ . Substituting Eq. (13) into Eq. (32), we obtain

$$\tilde{A}_{-i}(\phi) = \tilde{A}_i(\phi), \quad v_{-i} = v_i. \quad (33)$$

One can prove that the total skew polarization of all the positive (or negative) eigenbands

$$v := \sum_{i=1}^n v_i = \sum_{i=1}^n v_{-i} \quad (34)$$

is quantized in integers [79], and moreover,

$$v = \text{wind}(S) = \text{wind}(\det S) \in \mathbb{Z}. \quad (35)$$

Thus  $v_j$  characterizes the contribution to the winding number from the  $j$ th eigenband.

Here we make a few remarks. First, the polarization  $P_j$  and the skew polarization  $v_j$  are distinct quantities. However, there is a relation between the total polarization  $P$  and the total skew polarization  $v$  [79,80]:

$$P \equiv \frac{1}{2} (v \bmod 2). \quad (36)$$

Second, for a general system, the polarization  $P_j$  and the skew polarization  $v_j$  of a single band may not be quantized. Only the total polarization and the total skew polarization, summed over all the positive (or negative) bands, are quantized [82].

In Appendix C, we provide our detailed proofs for Eqs. (20), (21), (31), (35), and (36). Although these results are standard for chiral symmetric systems and can be found in e.g., Refs. [79,80,82], their proofs are scattered in the literature and some lack rigor. Our approach utilizes Jacobi's formula [83] to derive the results directly from the definitions, avoiding the need for introducing surface integrals of Berry curvatures as is commonly done. Additionally, the proof utilizes the existence of a periodic continuous singular value decomposition, which has been rigorously established in recent mathematical literature [84].

## B. Reciprocal systems

Our analysis above applies to general linear time-invariant systems. Now we focus on reciprocal systems and highlight their unique behaviors.

### 1. Autonne-Takagi decomposition

For a reciprocal system,  $S$  is a complex symmetric matrix [15,85,86]:

$$S = S^T. \quad (37)$$

We write  $S \in M_n^s$ , where  $M_n^s$  denotes set of  $n \times n$  complex symmetric matrices. Consequently, the singular value decomposition of  $S$  can take a special form:

$$S = U \Sigma U^T, \quad (38)$$

which is known as the *Autonne-Takagi decomposition* [41,87,88]. Comparing Eqs. (4) and (38), we see that for a reciprocal system, one can set

$$U = V^*, \quad \text{or} \quad v_i = u_i^*. \quad (39)$$

Thus the left singular vector  $v_i$  can be chosen as the time reversal of its corresponding right singular vector  $u_i$ . We refer to  $u_i$  as the *Takagi vectors*. Correspondingly, Eq. (6) becomes

$$S = \sum_{i=1}^n \sigma_i u_i u_i^T. \quad (40)$$

See Ref. [41] pp. 263–264 for more details about the Autonne-Takagi decomposition.

### 2. Block matrix with additional symmetries

For a reciprocal system with  $S \in M_n^s$ , the block Hermitian matrix

$$H = \begin{pmatrix} O & S^\dagger \\ S & O \end{pmatrix} = \begin{pmatrix} O & S^* \\ S & O \end{pmatrix}. \quad (41)$$

Besides the built-in chiral symmetry,  $H$  also possesses time-reversal symmetry,

$$\Sigma_x H^* \Sigma_x = H, \quad (42)$$

and particle-hole symmetry,

$$\Sigma_y H^* \Sigma_y = -H, \quad (43)$$

where

$$\Sigma_x = \begin{pmatrix} O & I \\ I & O \end{pmatrix}, \quad \Sigma_y = \begin{pmatrix} O & -iI \\ iI & O \end{pmatrix}. \quad (44)$$

Substituting Eq. (39) into Eq. (13), we obtain the eigenvectors of  $H$ :

$$|\psi_i\rangle = \frac{1}{\sqrt{2}} e^{i\alpha_i} \begin{pmatrix} u_i^* \\ u_i \end{pmatrix}, \quad |\psi_{-i}\rangle = \frac{1}{\sqrt{2}} e^{i\alpha_{-i}} \begin{pmatrix} u_i^* \\ -u_i \end{pmatrix}. \quad (45)$$

### 3. Quantized single-band polarization

These additional symmetries have topological consequences. We consider the same setting as Sec. (III A) and calculate the geometric phases of  $S \in M_n^s$  around a loop  $\gamma$  under the assumption of (23).<sup>2</sup>

The additional symmetries require the single-band polarization  $P_j$  to be quantized:

$$P_j \in \frac{1}{2} \mathbb{Z}_2, \quad j = \pm 1, \dots, \pm n. \quad (46)$$

<sup>2</sup>Condition (23) is generically met for reciprocal systems since for  $S \in M_n^s$ , having two equal singular values and having one zero singular value are both codimension 2 phenomena.

See Appendix D for proof of Eq. (46). In contrast, for nonreciprocal systems, we only have

$$P \in \frac{1}{2}\mathbb{Z}_2. \quad (47)$$

On the other hand, the additional symmetries do not lead to the quantization of the single-band skew polarization  $v_j$ . See numerical demonstrations in Sec. IV E.

#### 4. $\mathbb{Z}_2$ topology of Takagi vectors

There is another unique topological property of reciprocal systems:  $\mathbb{Z}_2$  topology of Takagi vectors. We consider the same setting above and study the evolution of  $S \in M_n^s$  around  $\boldsymbol{\gamma}$  under the assumption of (23). Then  $S(\boldsymbol{\gamma}(\phi))$  admits a continuous Autonne-Takagi decomposition [78]:

$$S(\boldsymbol{\gamma}(\phi)) = U(\phi)\Sigma(\phi)U^T(\phi), \quad \phi \in [0, 2\pi], \quad (48)$$

with  $U \in U(n)$  and  $\Sigma = \text{diag}(\sigma_1, \dots, \sigma_n)$ , where  $U(\phi)$ ,  $\Sigma(\phi)$  are as smooth as  $S(\boldsymbol{\gamma}(\phi))$ . See Ref. [78] for an algorithm that constructs the continuous Autonne-Takagi decomposition.

Continuity imposes a strong constraint on Autonne-Takagi decomposition. Without the requirement of continuity, at any given  $\phi$ ,  $U$  is unique only up to the sign of each column; thus there are  $2^n$  possibilities in total [41]. Continuity removes all the freedom: If we fix a reference factorization at some  $\phi$ , say at  $\phi = 0$ , then there is only one continuous factorization satisfying this given condition [78].

Such uniqueness has topological consequences. Consider a continuous Autonne-Takagi decomposition of  $S$  around  $\boldsymbol{\gamma}$  as given in Eq. (48). Since  $\boldsymbol{\gamma}(0) = \boldsymbol{\gamma}(2\pi)$ , we have

$$\Sigma(2\pi) = \Sigma(0), \quad |u_i(2\pi)\rangle = \pm |u_i(0)\rangle \quad (49)$$

where  $|u_i(\phi)\rangle$  denotes the  $i$ th column of  $U(\phi)$ . See Ref. [78] for proof of Eq. (49). The  $\pm$  sign defines a  $\mathbb{Z}_2$  topological number for  $|u_i\rangle$ , which is independent of the initial choice of  $U(0)$ . Since  $\mathbb{Z}_2$  is discrete, the sign persists under a small perturbation of  $\boldsymbol{\gamma}$ . The minus sign case corresponds to a flip of the Takagi vector around a loop, which is reminiscent of a flip of the normal vector of a Mobius strip after an orbit.

In contrast, the scattering matrix of a nonreciprocal system does not have the Autonne-Takagi decomposition. Therefore the singular vectors of a general scattering matrix do not have the  $\mathbb{Z}_2$  topology as described in Eq. (49).

## IV. TOPOLOGY OF COHERENT PERFECT ABSORPTION

In the previous section, we found that scattering matrices can have nontrivial topological properties in the parameter space. These topological properties impose strong constraints on the behaviors of scattering matrices and have direct physical consequences. As an application of our theory, in this section, we explore the connection between the topological winding of the scattering matrix and the physical effect of coherent perfect absorption (CPA).

Coherent perfect absorption refers to the complete absorption of light due to the interference of multiple incident waves. While this effect is well-known, its topological aspect has not been studied. Here we reveal the topological nature of coherent perfect absorption. We show that in a simply connected two-dimensional parameter space, a nonzero winding number of the scattering matrix along a simple loop implies the

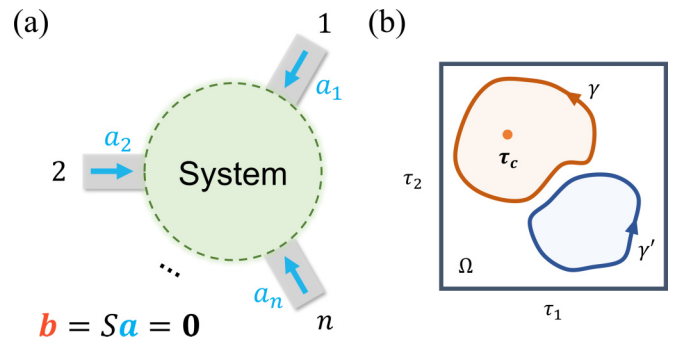


FIG. 3. Scheme of coherent perfect absorption. (a) System. (b) Parameter space.

existence of a CPA point within the loop where the system exhibits coherent perfect absorption. In the vicinity of this CPA point, the scattering matrix displays certain universal features: The smallest singular value forms a half Dirac cone in the parameter space with the apex reaching zero at the CPA point; the singular vectors exhibit nontrivial polarizations and skew-polarizations around the CPA point. Our findings elucidate the topology and universality of coherent perfect absorption.

### A. Coherent perfect absorption

We briefly review the concept of coherent perfect absorption [51,54]. Coherent perfect absorption refers to the complete absorption of light due to the interference of multiple incident waves. Consider an  $n$ -port linear time-invariant system as characterized by a scattering matrix  $S \in M_n$  [Fig. 3(a)]. The system is a coherent perfect absorber if there exists an input  $\mathbf{a} \in \mathbb{C}^n \setminus \{\mathbf{0}\}$  such that

$$S\mathbf{a} = \mathbf{0}, \quad (50)$$

and thus the absorptivity of the input

$$\alpha[\mathbf{a}] := 1 - \frac{\mathbf{a}^\dagger S^\dagger S \mathbf{a}}{\mathbf{a}^\dagger \mathbf{a}} = 1. \quad (51)$$

### B. Codimension of CPA

From Eq. (50), a necessary and sufficient condition of coherent perfect absorption is

$$\det S = 0, \quad (52)$$

or equivalently,

$$\sigma_n = 0. \quad (53)$$

Thus coherent perfect absorption is an effect of codimension 2. This codimension result remains the same for reciprocal systems with  $S \in M_n^s$ .

### C. Topology of a generic CPA point

Since coherent perfect absorption has a codimension of 2, one typically needs to adjust two real parameters to achieve it. Hence, we consider a system described by an  $n \times n$  scattering matrix  $S$  that depends on two parameters  $\boldsymbol{\tau} = (\tau_1, \tau_2) \in \Omega$ , where  $\Omega$  is a compact and simply connected subset of  $\mathbb{R}^2$ . The system is characterized by the map  $S : \boldsymbol{\tau} \mapsto S(\boldsymbol{\tau})$  as given

in Eq. (15). We assume that  $S$  is continuous. In the two-dimensional parameter space  $\Omega$ , coherent perfect absorption generically occurs at isolated points, referred to as *CPA points*. Without loss of generality, we assume that there is a unique generic CPA point  $\tau_c = (\tau_{c1}, \tau_{c2}) \in \Omega$ , and there is no other point in  $\Omega$  where a pair of singular values coalesce or a singular value becomes zero.<sup>3</sup> We introduce two simple closed curves in  $\Omega$ : a nontrivial loop  $\gamma$  that encircles  $\tau_c$  and a trivial loop  $\gamma'$  that does not. Figure 3(b) shows a scheme of the parameter space.

Now we study the singular topology of the  $S$  matrix near a generic CPA point. We apply our general theory and obtain the following topological results.

### 1. General systems with $S \in M_n$

Along a nontrivial loop  $\gamma$ :

$$\text{wind}(S) = \nu = \pm 1, \quad P \equiv \frac{1}{2}. \quad (54)$$

In contrast, along a trivial loop  $\gamma'$ :

$$\text{wind}(S) = \nu = 0, \quad P \equiv 0. \quad (55)$$

### 2. Reciprocal systems with $S \in M_n^*$

In addition to Eqs. (54) and (55), we have further results. Along a nontrivial loop  $\gamma$ :

$$P_n = P_{-n} \equiv \frac{1}{2}; \quad P_j \equiv 0, \quad j = \pm 1, \pm 2, \dots, \pm(n-1). \quad (56)$$

$$|u_n(2\pi)\rangle = -|u_n(0)\rangle; \quad |u_i(2\pi)\rangle = |u_i(0)\rangle, \quad i = 1, 2, \dots, n-1. \quad (57)$$

In contrast, along a trivial loop  $\gamma'$ :

$$P_j \equiv 0, \quad j = \pm 1, \dots, \pm n. \quad (58)$$

$$|u_i(2\pi)\rangle = |u_i(0)\rangle, \quad i = 1, \dots, n. \quad (59)$$

See Appendix E for proof of these results.

### D. Effective two-band model

To better understand the physics, we develop an effective two-band model near a generic CPA point using the matrix perturbation theory [69,89]. The key quantities for coherent perfect absorption are the smallest singular value of the  $S$  matrix  $\sigma_n$  and the corresponding right singular vector  $v_n$ . This is because for a given  $S \in M_n$ , the maximal absorptivity for all possible coherent input  $\mathbf{a} \in \mathbb{C}^n \setminus \{\mathbf{0}\}$  is

$$\max \alpha[\mathbf{a}] = 1 - \sigma_n^2, \quad (60)$$

which is obtained by the input

$$\mathbf{a} = cv_n, \quad c \in \mathbb{C}^*. \quad (61)$$

So we study the generic behaviors of  $\sigma_n$  and  $v_n$  near a CPA point  $\tau_c$ . Recall that  $\sigma_n(\tau_c) = 0$ .

We consider a small simple loop  $\gamma$  encircling  $\tau_c$  such that

$$\|S(\boldsymbol{\tau}) - S(\tau_c)\| \ll \sigma_{n-1}(\tau_c), \quad \forall \boldsymbol{\tau} \in \Omega_\gamma, \quad (62)$$

where  $\|M\| := \sigma_{\max}(M)$  denotes the spectral norm of  $M \in M_n$  [41], and  $\Omega_\gamma \subset \Omega$  is the area enclosed by  $\gamma$ . Then we can treat  $S(\boldsymbol{\tau})$  as a perturbation of  $S(\tau_c)$ . Using the block matrix technique, we obtain a more familiar perturbation problem of the Hermitian matrix [89–91]:

$$H(\boldsymbol{\tau}) = H(\tau_c) + \delta H(\boldsymbol{\xi}) \quad (63)$$

where  $\boldsymbol{\xi} := \boldsymbol{\tau} - \tau_c$ .  $H(\tau_c)$  has doubly degenerate zero eigenvalues

$$\lambda_n(\tau_c) = \lambda_{-n}(\tau_c) = 0 \quad (64)$$

with the eigenvectors  $|\psi_n^0\rangle$  and  $|\psi_{-n}^0\rangle$ , respectively. We use the degenerate perturbation theory [92,93] to obtain the effective two-band model in the subspace spanned by  $|\psi_n^0\rangle$  and  $|\psi_{-n}^0\rangle$ . Since  $\delta H$  has the chiral symmetry as described by Eq. (8), the effective Hermitian matrix must take the form

$$H_{\text{eff}}(\boldsymbol{\xi}) = \begin{pmatrix} 0 & f^*(\boldsymbol{\xi}) \\ f(\boldsymbol{\xi}) & 0 \end{pmatrix}, \quad (65)$$

where  $f(\mathbf{0}) = 0$ . We take the first-order expansion of  $f(\boldsymbol{\xi})$ :

$$f(\boldsymbol{\xi}) = c_1 \xi_1 + c_2 \xi_2 + O(\boldsymbol{\xi}^2) \quad (66)$$

where  $c_1, c_2 \in \mathbb{C}$ . Generically,  $c_1$  and  $c_2$  are nonzero and linearly independent over  $\mathbb{R}$ . Then

$$H_{\text{eff}}(\boldsymbol{\xi}) = \begin{pmatrix} 0 & c_1^* \xi_1 + c_2^* \xi_2 \\ c_1 \xi_1 + c_2 \xi_2 & 0 \end{pmatrix} = \sum_{i,j=1}^2 \xi_i J_{ij} s_j, \quad (67)$$

where  $s_j$  denote the Pauli matrices, and

$$J := \begin{pmatrix} c_{1r} & c_{1i} \\ c_{2r} & c_{2i} \end{pmatrix} \in M_2(\mathbb{R}), \quad (68)$$

where  $c_{1r}$  and  $c_{1i}$  are the real and imaginary parts of  $c_1$ , etc. From Eq. (67), we determine the band dispersion

$$\lambda_{\pm n}(\boldsymbol{\xi}) = \pm |c_1 \xi_1 + c_2 \xi_2| = \pm \sqrt{\sum_{i,j,k=1}^2 J_{ik} J_{jk} \xi_i \xi_j}. \quad (69)$$

Translating  $H$  back to  $S$ , we obtain

$$\sigma_n(\boldsymbol{\xi}) = \lambda_n(\boldsymbol{\xi}) = |c_1 \xi_1 + c_2 \xi_2|. \quad (70)$$

Figures 4(a) and 4(b) show typical spectra of  $\sigma_n(\boldsymbol{\xi})$  and  $\lambda_{\pm n}(\boldsymbol{\xi})$  near a generic CPA point. We see that  $\sigma_n(\boldsymbol{\xi})$  forms an upright anisotropic half Dirac cone, while  $\lambda_{\pm n}(\boldsymbol{\xi})$  form an upright Dirac cone. Dirac cones have well-known nontrivial topology [94–96]. Such topological features are directly connected with the topological results discussed in Sec. IV C. For example, direct calculation shows that

$$2P \equiv \text{wind}(S) = \text{sgn}(\det J). \quad (71)$$

The effective two-band model in Eq. (67) remains unchanged if the system is further assumed to be reciprocal. Thus reciprocal and nonreciprocal systems exhibit similar behaviors near a CPA point. Their differences appear when

<sup>3</sup>Generic means that we neglect any effects of higher codimension such as the coalescing of two CPA points. See Ref. [112] for a more rigorous elaboration.

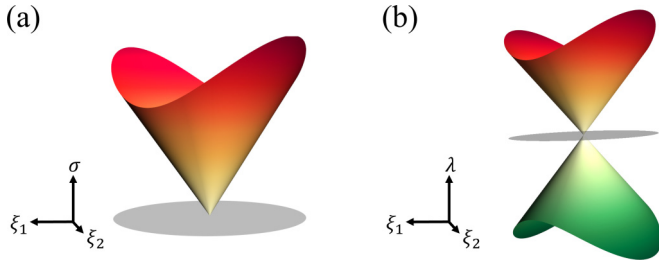


FIG. 4. The effective two-band model with parameters  $c_1 = 5 + 1i$ ,  $c_2 = -3 + 4i$ . The colored surfaces represent the spectra of  $H_{\text{eff}}$  in Eq. (67). The gray plane indicates the zero value. (a) The singular value  $\sigma_n(\xi)$  in Eq. (70). (b) The eigenvalues  $\lambda_{\pm n}(\xi)$  in Eq. (69).

the loop  $\gamma$  is far from the CPA point such that the contributions from other bands become nonnegligible.

### E. Numerical demonstration

We demonstrate the topology of coherent perfect absorption as discussed above with three concrete physical examples. We illustrate the universal features of generic CPA points and highlight the similarities and differences between reciprocal and nonreciprocal systems.

#### 1. 2-port reciprocal CPA system

The first example is a 2-port reciprocal system. The structure is a double-layer dielectric slab [Fig. 5(a)]. Each layer has a thickness of  $d = 1 \mu\text{m}$ . The first layer has a scalar relative permittivity  $\varepsilon = \varepsilon_r + i\varepsilon_i$ , where  $\varepsilon_r = 6.0$  and  $\varepsilon_i \in [0, 1.5]$ . The second layer has a scalar relative permittivity  $\varepsilon' = 3.0$ . The structure is illuminated by linearly polarized light in the normal direction from both sides. The light frequency  $f = \omega/2\pi \in [285, 300]$  THz. The system is characterized by a  $2 \times 2$  scattering matrix

$$S(f, \varepsilon_i) = \begin{pmatrix} r_1 & t \\ t & r_2 \end{pmatrix}. \quad (72)$$

We calculate  $S(f, \varepsilon_i)$  using the transfer matrix method [97]. Figures 5(b) and 5(c) plot the logarithmic amplitude and phase of  $\det S$ , respectively. There is a single CPA point ( $f = 249.6$  THz,  $\varepsilon_i = 0.815$ ) with a winding number

$$\text{wind}(S) = +1. \quad (73)$$

We introduce two square loops  $\gamma(\phi)$  and  $\gamma'(\phi)$ , where  $\phi \in [0, 2\pi]$  denotes the angle around the center of the square with the lower left corner corresponding to  $\phi = 0$ .  $\gamma$  encircles the CPA point, while  $\gamma'$  does not.

Figure 5(d) plots the singular values  $\sigma_1(f, \varepsilon_i)$  and  $\sigma_2(f, \varepsilon_i)$ .  $\sigma_2(f, \varepsilon_i)$  forms a half Dirac cone. From  $S$ , we construct  $H$  using the block matrix technique. Figure 5(e) plots the eigenvalues of  $H$ :  $\lambda_{\pm 1}(H) = \pm\sigma_1(S)$ ,  $\lambda_2(H)$  and  $\lambda_{-2}(H)$  form an upright Dirac cone that touches at the CPA point. The dispersion is linear near the CPA point.

We calculate the continuous Autonne-Takagi decomposition of  $S$  and obtain the Takagi vectors  $|u_1\rangle$  and  $|u_2\rangle$  along  $\gamma$  and  $\gamma'$ . Figures 5(f) and 5(g) plot

$$\text{Re} \langle u_i(\phi) | u_i(0) \rangle, \quad i = 1, 2, \quad (74)$$

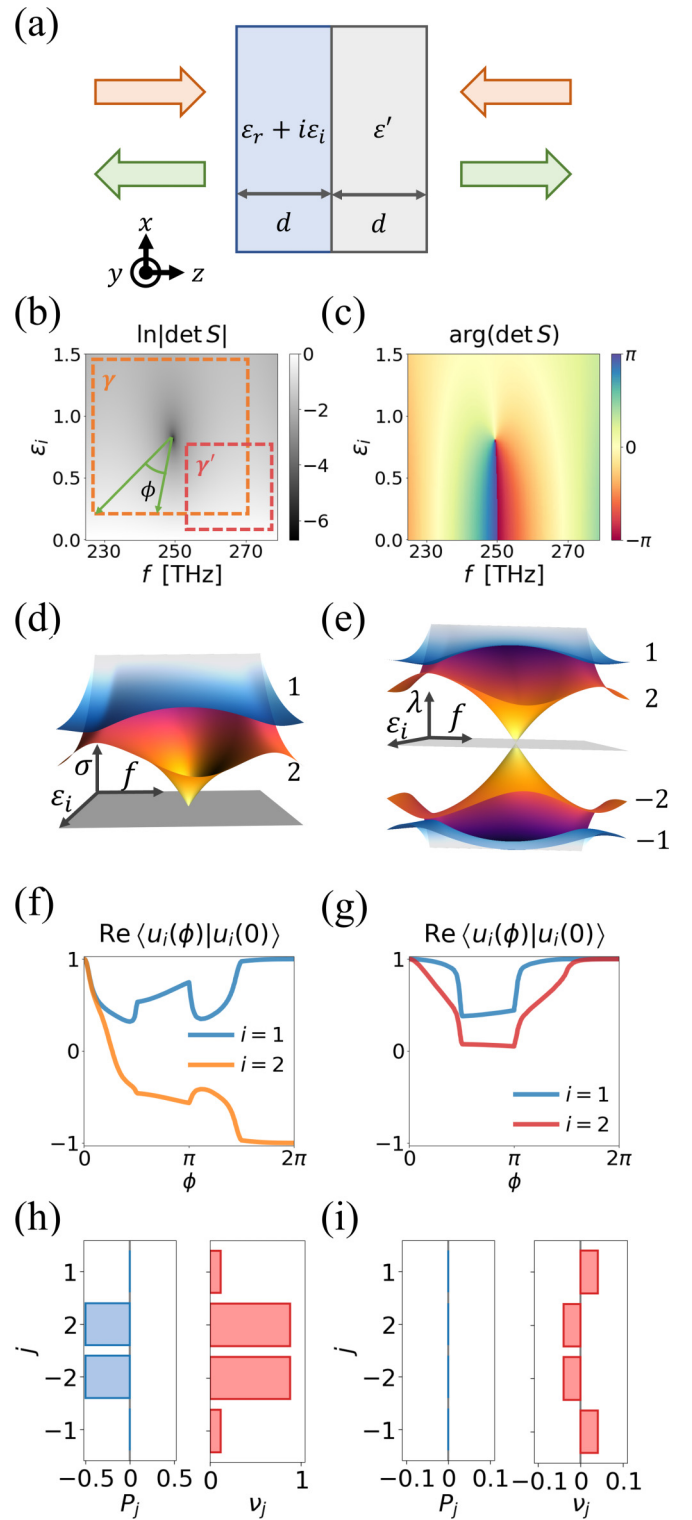


FIG. 5. A 2-port reciprocal CPA system. (a) Structure. (b)  $\ln|\det S|(f, \varepsilon_i)$ .  $\gamma(\phi)$  and  $\gamma'(\phi)$  are two loops. (c)  $\arg(\det S)(f, \varepsilon_i)$ . (d)  $\sigma_i(f, \varepsilon_i)$ ,  $i = 1, 2$ . (e)  $\lambda_j(f, \varepsilon_i)$ ,  $j = \pm 1, \pm 2$ . (f)  $\text{Re} \langle u_i(\phi) | u_i(0) \rangle$  along  $\gamma$ . (g)  $\text{Re} \langle u_i(\phi) | u_i(0) \rangle$  along  $\gamma'$ . (h)  $P_j$  and  $v_j$  around  $\gamma$ . (i)  $P_j$  and  $v_j$  around  $\gamma'$ .

along  $\gamma$  and  $\gamma'$ , respectively. We see that  $|u_2\rangle$  changes sign along  $\gamma$  but not  $\gamma'$ , while  $|u_1\rangle$  does not change sign in either case. These results confirm Eqs. (57) and (59).



Figure 5(h) plots the polarization  $P_j$  and the skew polarization  $v_j$  around  $\boldsymbol{\gamma}$ . We observe that

$$P_1 = P_{-1} \equiv 0, \quad P_2 = P_{-2} \equiv \frac{1}{2}, \quad (75)$$

which confirms Eq. (56). (Note that  $-\frac{1}{2} \equiv \frac{1}{2}$ .) In contrast,

$$v_j \neq 0, \quad \text{for all } j. \quad (76)$$

The total polarization and skew polarization

$$P = \sum_{i=1}^2 P_i \equiv \frac{1}{2}, \quad v = \sum_{i=1}^2 v_i = 1, \quad (77)$$

which confirm Eq. (54).

Figure 5(i) plots the polarization  $P_j$  and the skew polarization  $v_j$  around  $\boldsymbol{\gamma}'$ . We observe that

$$P_j \equiv 0, \quad \text{for all } j. \quad (78)$$

which confirms Eq. (58). In contrast,

$$v_j \neq 0, \quad \text{for all } j. \quad (79)$$

The total polarization and skew polarization

$$P = \sum_{i=1}^2 P_i \equiv 0, \quad v = \sum_{i=1}^2 v_i = 0, \quad (80)$$

which confirm Eq. (55).

## 2. 4-port reciprocal CPA system

The second example is a 4-port reciprocal system. The structure is a single-layer bianisotropic slab with a thickness  $d = 1 \mu\text{m}$  [Fig. 6(a)]. The material is characterized by a  $6 \times 6$  constitutive matrix  $C$  such that

$$\begin{pmatrix} \mathbf{D} \\ \mathbf{B} \end{pmatrix} = C \begin{pmatrix} \mathbf{E} \\ \mathbf{H} \end{pmatrix} = \begin{pmatrix} \varepsilon_0 \varepsilon & \sqrt{\varepsilon_0 \mu_0} \zeta \\ \sqrt{\varepsilon_0 \mu_0} \eta & \mu_0 \mu \end{pmatrix} \begin{pmatrix} \mathbf{E} \\ \mathbf{H} \end{pmatrix}, \quad (81)$$

where  $\varepsilon_0$  and  $\mu_0$  are the vacuum permittivity and permeability, respectively;  $\varepsilon$ ,  $\mu$ ,  $\zeta$ ,  $\eta$  are  $3 \times 3$  matrices of relative electric permittivity, magnetic permeability, electric-magnetic coupling strength, and magnetoelectric coupling strength, respectively. We randomly set

$$\varepsilon = \varepsilon_r + i\varepsilon_i = \begin{pmatrix} 1.75 & 0.30 & 0.09 \\ 0.30 & 1.97 & 1.11 \\ 0.09 & 1.11 & 4.33 \end{pmatrix} + i\kappa \begin{pmatrix} 0.72 & -0.17 & -0.05 \\ -0.17 & 0.65 & -0.26 \\ -0.05 & -0.26 & 0.78 \end{pmatrix}, \quad (82)$$

$$\mu = \begin{pmatrix} 1.08 & -0.28 & -0.07 \\ -0.28 & 1.02 & 0.11 \\ -0.07 & 0.11 & 0.70 \end{pmatrix},$$

$$\zeta = -\eta^T = i \begin{pmatrix} 0.36 & 0.11 & 0.40 \\ 0.57 & 0.15 & 0.57 \\ 0.40 & 0.06 & 0.27 \end{pmatrix}, \quad (83)$$

where

$$\kappa = \|\varepsilon_i\| \in [0, 1.5] \quad (84)$$

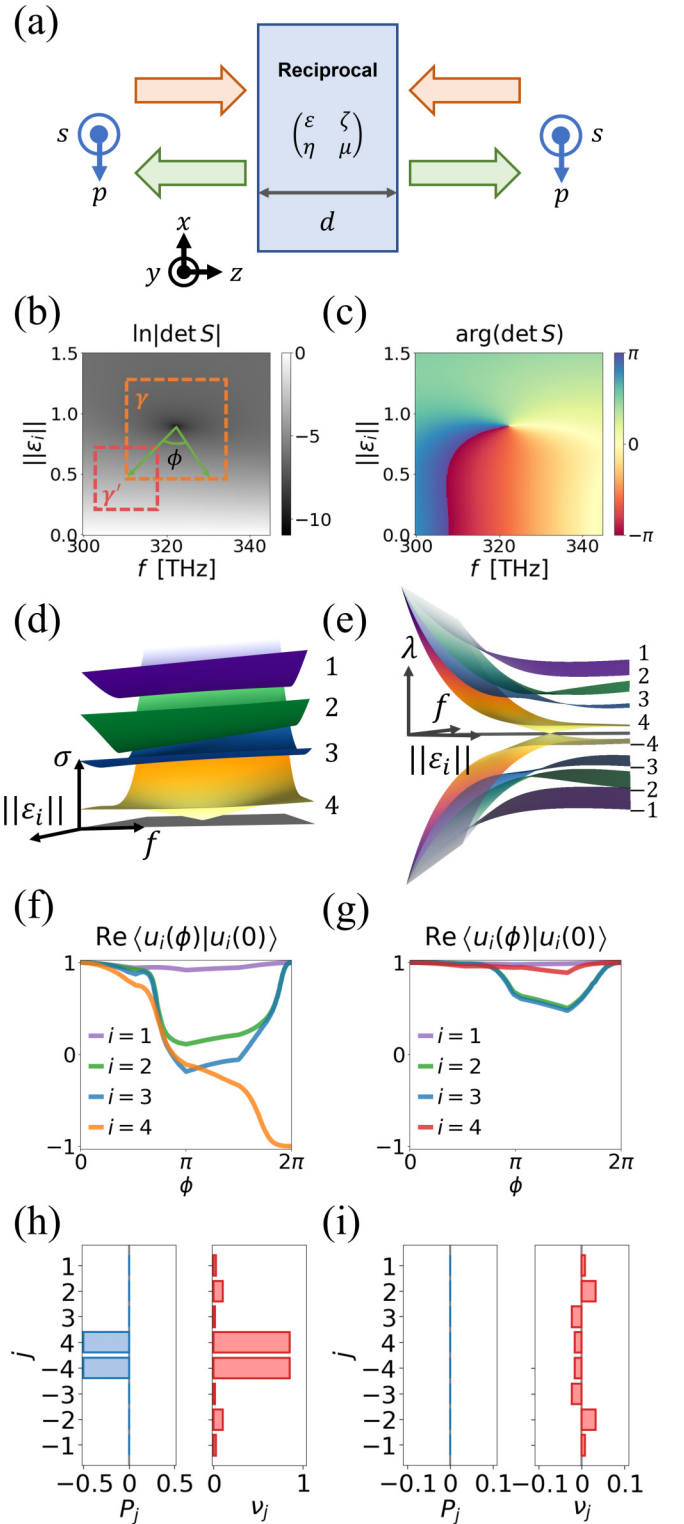


FIG. 6. A 4-port reciprocal CPA system. (a) Structure. (b)  $\ln|\det S|(f, \|\varepsilon_i\|)$ . (c)  $\arg(\det S)(f, \|\varepsilon_i\|)$ . (d)  $\sigma_i(f, \|\varepsilon_i\|)$ ,  $1 \leq i \leq 4$ . (e)  $\lambda_j(f, \|\varepsilon_i\|)$ ,  $j = \pm i$ . (f)  $\text{Re}\langle u_i(\phi)|u_i(0)\rangle$  along  $\boldsymbol{\gamma}$ . (g)  $\text{Re}\langle u_i(\phi)|u_i(0)\rangle$  along  $\boldsymbol{\gamma}'$ . (h)  $P_j$  and  $v_j$  around  $\boldsymbol{\gamma}$ . (i)  $P_j$  and  $v_j$  around  $\boldsymbol{\gamma}'$ .

measures the overall strength of the material loss. The material is reciprocal since

$$\varepsilon = \varepsilon^T, \quad \mu = \mu^T, \quad \zeta = -\eta^T. \quad (85)$$

The structure is illuminated by the light of both polarizations in the normal direction from both sides. The light frequency  $f = \omega/2\pi \in [300, 345]$  THz. The system is characterized by a  $4 \times 4$  scattering matrix

$$S(f, \|\varepsilon_i\|) = \begin{pmatrix} r_{ss}^F & r_{sp}^F & t_{ss}^B & t_{sp}^B \\ r_{ps}^F & r_{pp}^F & t_{ps}^B & t_{pp}^B \\ t_{ss}^F & t_{sp}^F & r_{ss}^B & r_{sp}^B \\ t_{ps}^F & t_{pp}^F & r_{ps}^B & r_{pp}^B \end{pmatrix}, \quad (86)$$

where for examples  $r_{sp}^F$  denotes the reflection coefficient for a forward-propagating  $p$  polarized light into the reflected  $s$  polarized light, and  $t_{ps}^B$  denotes the transmission coefficient for a backward-propagating  $s$  polarized light into the transmitted  $p$  polarized light. Here the electric fields of the  $p$  and  $s$  polarized light are aligned with the  $-x$  and  $y$  directions, respectively [Fig. 6(a)]. See Appendix F for more explanations about the basis convention.

We calculate  $S(f, \|\varepsilon_i\|)$  using the transfer matrix method. Figures 6(b) and 6(c) plot the logarithmic amplitude and phase of  $\det S$ , respectively. There is a single CPA point ( $f = 322$  THz,  $\|\varepsilon_i\| = 0.895$ ) with a winding number

$$\text{wind}(S) = +1. \quad (87)$$

We introduce a nontrivial square loop  $\gamma(\phi)$  and a trivial square loop  $\gamma'(\phi)$ .

Figure 6(d) plots the singular values  $\sigma_i(f, \|\varepsilon_i\|)$ ,  $1 \leq i \leq 4$ .  $\sigma_4(f, \|\varepsilon_i\|)$  forms a half Dirac cone. From  $S$ , we construct  $H$  using the block matrix technique. Figure 6(e) plots the eigenvalues of  $H$ .  $\lambda_4(H)$  and  $\lambda_{-4}(H)$  form an upright Dirac cone.

We calculate the continuous Autonne-Takagi decomposition of  $S$  and obtain the Takagi vectors  $|u_i\rangle$ ,  $1 \leq i \leq 4$ , along  $\gamma$  and  $\gamma'$ . Figures 6(f) and 6(g) plot

$$\text{Re} \langle u_i(\phi) | u_i(0) \rangle, \quad 1 \leq i \leq 4, \quad (88)$$

along  $\gamma$  and  $\gamma'$ , respectively.  $|u_4\rangle$  changes sign along  $\gamma$  but not  $\gamma'$ , while the other Takagi vectors do not change signs in either case. These results confirm Eqs. (57) and (59).

Figure 6(h) plots the polarization  $P_j$  and skew polarization  $v_j$  around  $\gamma$ . We observe that

$$P_4 = P_{-4} \equiv \frac{1}{2}; \quad P_j \equiv 0, \quad \text{for other } j. \quad (89)$$

which confirms Eq. (56). In contrast,

$$v_j \neq 0, \quad \text{for all } j. \quad (90)$$

The total polarization and skew polarization

$$P = \sum_{i=1}^4 P_i \equiv \frac{1}{2}, \quad v = \sum_{i=1}^4 v_i = 1, \quad (91)$$

which confirm Eq. (54).

Figure 6(i) plots the polarization  $P_j$  and the skew polarization  $v_j$  around  $\gamma'$ . We observe that

$$P_j \equiv 0, \quad \text{for all } j. \quad (92)$$

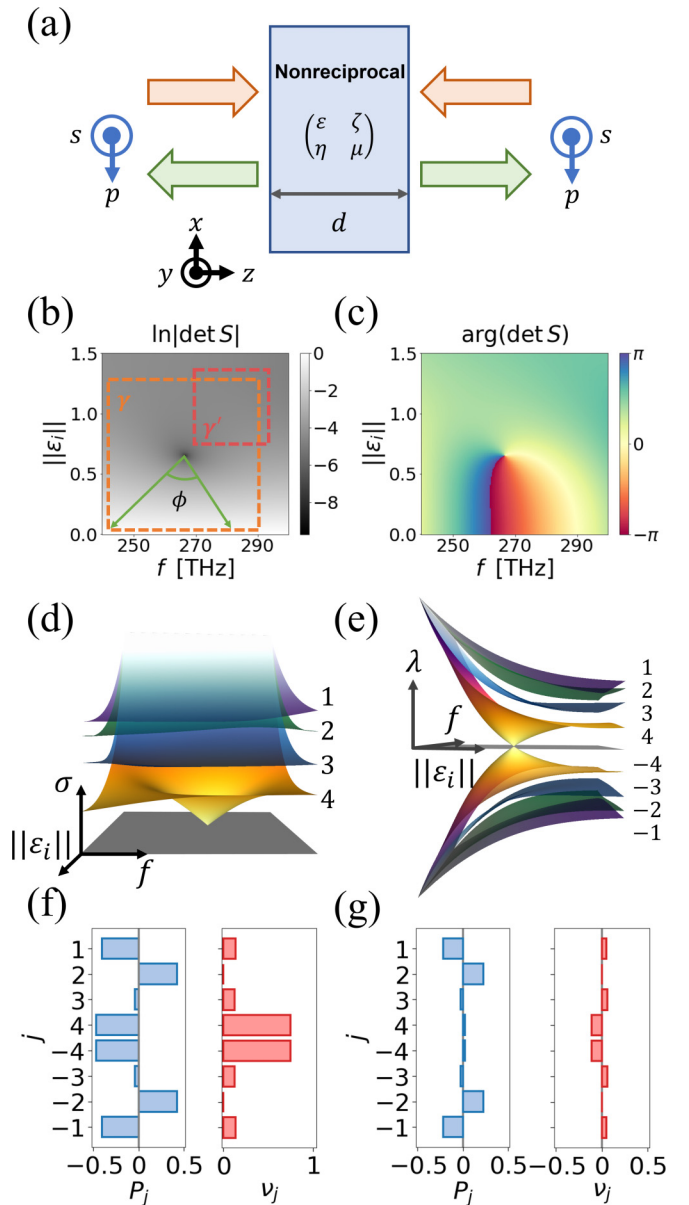


FIG. 7. A 4-port nonreciprocal CPA system. (a) Structure. (b)  $\ln|\det S|(f, \|\varepsilon_i\|)$ . (c)  $\arg(\det S)(f, \|\varepsilon_i\|)$ . (d)  $\sigma_i(f, \|\varepsilon_i\|)$ ,  $1 \leq i \leq 4$ . (e)  $\lambda_j(f, \|\varepsilon_i\|)$ ,  $j = \pm i$ . (f)  $P_j$  and  $v_j$  around  $\gamma$ . (g)  $P_j$  and  $v_j$  around  $\gamma'$ .

which confirms Eq. (58). In contrast,

$$v_j \neq 0, \quad \text{for all } j. \quad (93)$$

The total polarization and skew polarization

$$P = \sum_{i=1}^4 P_i \equiv 0, \quad v = \sum_{i=1}^4 v_i = 0, \quad (94)$$

which confirm Eq. (55).

### 3. 4-port nonreciprocal CPA system

The third example is a 4-port nonreciprocal system. The structure is a single-layer bianisotropic slab with a thickness of  $d = 1 \mu\text{m}$  [Fig. 7(a)]. The material has relative constitutive

tensors

$$\varepsilon = \varepsilon_r + i\varepsilon_i, \quad (95)$$

$$\varepsilon_r = \begin{pmatrix} 2.13 & -0.44 + 1.06i & -0.61 + 0.41i \\ -0.44 - 1.06i & 3.07 & 0.94 + 0.64i \\ -0.61 - 0.41i & 0.94 - 0.64i & 2.85 \end{pmatrix}, \quad (96)$$

$$\varepsilon_i = \kappa \begin{pmatrix} 0.84 & -0.13 + 0.17i & -0.06 - 0.20i \\ -0.13 - 0.17i & 0.70 & 0.16 - 0.24i \\ -0.06 + 0.20i & 0.16 + 0.24i & 0.72 \end{pmatrix}, \quad (97)$$

$$\mu = \begin{pmatrix} 0.81 & 0.01 + 0.19i & 0.13 + 0.06i \\ 0.01 - 0.19i & 0.94 & 0.15 - 0.20i \\ 0.13 - 0.06i & 0.15 + 0.20i & 1.06 \end{pmatrix}, \quad (98)$$

$$\zeta = \eta^\dagger = \begin{pmatrix} 0.12 + 0.16i & 0.15 + 0.25i & -0.20 + 0.16i \\ -0.07 - 0.05i & 0.11 - 0.08i & 0.16 - 0.18i \\ -0.08 - 0.33i & 0.19 + 0.30i & -0.01 - 0.16i \end{pmatrix}. \quad (99)$$

where  $\kappa = \|\varepsilon_i\| \in [0, 1.5]$  measures the overall strength of the material loss. The material is lossless when  $\kappa = 0$  and is lossy when  $\kappa > 0$ . The material is nonreciprocal since

$$\varepsilon \neq \varepsilon^T, \quad \mu \neq \mu^T, \quad \zeta \neq -\eta^T. \quad (100)$$

The structure is illuminated by the light of both polarizations in the normal direction from both sides. The light frequency  $f = \omega/2\pi \in [240, 300]$  THz. The system is characterized by a  $4 \times 4$  scattering matrix  $S(f, \|\varepsilon_i\|)$  with the same form of Eq. (86).

We calculate  $S(f, \|\varepsilon_i\|)$  using the transfer matrix method. Figures 7(b) and 7(c) plot the logarithmic amplitude and phase of  $\det S$ , respectively. There is a single CPA point ( $f = 266.6$  THz,  $\|\varepsilon_i\| = 0.6525$ ) with a winding number

$$\text{wind}(S) = +1. \quad (101)$$

We introduce a nontrivial square loop  $\boldsymbol{\gamma}(\phi)$  and a trivial square loop  $\boldsymbol{\gamma}'(\phi)$ .

Figure 7(d) plots the singular values  $\sigma_i(f, \varepsilon_i)$ ,  $1 \leq i \leq 4$ .  $\sigma_4(f, \|\varepsilon_i\|)$  forms a half Dirac cone. From  $S$ , we construct  $H$  using the block matrix technique. Figure 7(e) plots the eigenvalues of  $H$ .  $\lambda_4(H)$  and  $\lambda_{-4}(H)$  form an upright Dirac cone. The system is nonreciprocal and thus does not have the Autonne-Takagi decomposition.

Figure 7(f) plots the polarization  $P_j$  and the skew polarization  $v_j$  around  $\boldsymbol{\gamma}$ . We observe that

$$P_j \neq 0 \quad \text{for all } j. \quad (102)$$

Thus all the eigenbands exhibit nontrivial Berry phases. This is a unique nonreciprocal effect [cf. Eq. (56)]. We also see that

$$v_j \neq 0 \quad \text{for all } j, \quad (103)$$

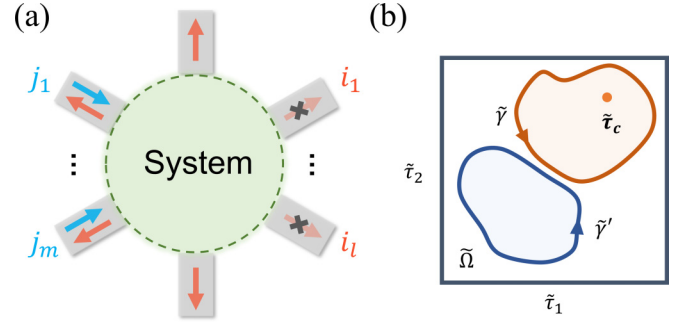


FIG. 8. Scheme of coherent perfect extinction. (a) System. (b) Parameter space.

which is similar to reciprocal systems. The total polarization and skew polarization

$$P = \sum_{i=1}^4 P_i \equiv \frac{1}{2}, \quad v = \sum_{i=1}^4 v_i = 1, \quad (104)$$

which confirm Eq. (54).

Figure 7(g) plots the polarization  $P_j$  and the skew polarization  $v_j$  around  $\boldsymbol{\gamma}'$ . We observe that

$$P_j \neq 0, \quad \text{for all } j. \quad (105)$$

This is a unique nonreciprocal effect [cf. Eq. (58)]. We also see that

$$v_j \neq 0, \quad \text{for all } j. \quad (106)$$

The total polarization and skew polarization

$$P = \sum_{i=1}^4 P_i \equiv 0, \quad v = \sum_{i=1}^4 v_i = 0, \quad (107)$$

which confirm Eq. (55).

## V. TOPOLOGY OF COHERENT PERFECT EXTINCTION

In the preceding section, we found that the effect of coherent perfect absorption is connected to the topological winding of the scattering matrix. This prompts us to investigate other scattering phenomena with topological nature. As an example, we inquire about the physical effect that is connected to the topological winding of a scattering *submatrix*. The outcome is a new phenomenon we term coherent perfect extinction (CPE). Coherent perfect extinction refers to the complete extinction of light due to the interference of multiple incident waves. It encompasses many known effects as special cases, including complete polarization conversion [25] and reflectionless scattering modes [60–62]. In this section, we study coherent perfect extinction and reveal its topological nature.

### A. Coherent perfect extinction

We introduce the concept of coherent perfect extinction. Consider an  $n$ -port linear time-invariant system as characterized by a scattering matrix  $S \in M_n$  [Fig. 8(a)]. We select  $m$  input ports with indices  $j_1, \dots, j_m$  and  $l$  output ports with indices  $i_1, \dots, i_l$ , where  $1 \leq l, m \leq n$ . (The two sets  $\{j_k\}$  and  $\{i_k\}$  may or may not have intersection.) The scattering from the

selected input to selected output ports is then characterized by a *scattering submatrix*:

$$\tilde{S} := S[i_1, \dots, i_l; j_1, \dots, j_m], \quad (108)$$

which is the  $l \times m$  submatrix of  $S$  keeping only the  $\{i_k\}$ th rows and  $\{j_k\}$ th columns. We consider light scattered into the unselected  $(n - l)$  output ports as scattering loss.

We say that the system exhibits coherent perfect extinction if there exists an input  $\tilde{\mathbf{a}} \in \mathbb{C}^m \setminus \{\mathbf{0}\}$  such that

$$\tilde{S}\tilde{\mathbf{a}} = \mathbf{0}, \quad (109)$$

and thus the extinction coefficient [98,99] of the input

$$\epsilon[\tilde{\mathbf{a}}] := 1 - \frac{\tilde{\mathbf{a}}^\dagger \tilde{S}^\dagger \tilde{S} \tilde{\mathbf{a}}}{\tilde{\mathbf{a}}^\dagger \tilde{\mathbf{a}}} = 1. \quad (110)$$

Coherent perfect extinction is a natural extension of coherent perfect absorption [cf. Eqs. (50) and (51)]. However, these two effects are fundamentally different, since extinction consists of both absorption and scattering losses [98,99]. The concept of “mutual extinction and transparency,” i.e., the enhanced or reduced extinction by constructive or destructive interference of multiple incident waves, has been recently proposed and demonstrated in Refs. [100–102]. However, coherent *perfect* extinction has not been proposed or demonstrated.

There are many choices for the scattering submatrix  $\tilde{S}$ . A matrix  $S \in M_n$  has  $(2^n - 1)^2$  submatrices and  $\binom{2^n}{n} - 1$  square submatrices (see Ref. [81], pp. 169 for combinatorial proof). We note three special cases. (1) When  $l = m = 1$ ,  $\tilde{S}$  reduces to a single element of  $S$ . The topology of this special case has been studied in, e.g., Refs. [25,33]. (2) When  $l = m = n$ ,  $\tilde{S} = S$ , and coherent perfect extinction reduces to coherent perfect absorption. (3) When  $l = m$  and  $\{i_k\} = \{j_k\}$ ,  $\tilde{S}$  is a principal submatrix of  $S$ , and coherent perfect extinction reduces to coherent zero reflection. This special case corresponds to the recently proposed “reflectionless scattering modes” [60–62]; yet, its topology has not been studied. Therefore the concept of coherent perfect extinction generalizes many known physical effects and points to a unified theory for all these effects.

### B. Codimension of CPE

Unlike coherent perfect absorption which always has a codimension of 2, the codimension of coherent perfect extinction depends on the numbers of selected output ports  $l$  and selected input ports  $m$ .

When  $l < m$ , coherent perfect extinction is always attainable. This is because

$$\text{nullity}(\tilde{S}) = m - \text{rank}(\tilde{S}) \geq m - l > 0, \quad (111)$$

hence Eq. (109) must have nontrivial solutions. Thus in this case,  $\text{codim}(\text{CPE}) = 0$ .

When  $l = m$ , coherent perfect extinction has a codimension of 2. This is because  $\tilde{S} \in M_m$  is a square submatrix of  $S$ , and coherent perfect extinction occurs if and only if

$$\det \tilde{S} = 0, \quad (112)$$

or equivalently,

$$\tilde{\sigma}_m = 0, \quad (113)$$

where  $\tilde{\sigma}_m$  is the smallest singular value of  $\tilde{S}$ . Thus, in this case,  $\text{codim}(\text{CPE}) = 2$ .

When  $l > m$ , coherent perfect extinction has a codimension of  $2(l - m) + 2$ . This is because we can partition  $\tilde{S}$  as

$$\tilde{S} = \begin{pmatrix} \tilde{S}_\alpha \\ \tilde{S}_\beta \end{pmatrix}, \quad (114)$$

where  $\tilde{S}_\alpha$  and  $\tilde{S}_\beta$  are  $m \times m$  and  $(l - m) \times m$  matrices, respectively. Then Eq. (109) becomes

$$\tilde{S}\tilde{\mathbf{a}} = \mathbf{0} \iff \begin{cases} \tilde{S}_\alpha \tilde{\mathbf{a}} = \mathbf{0}, \\ \tilde{S}_\beta \tilde{\mathbf{a}} = \mathbf{0}. \end{cases} \quad (115)$$

The first set of equations requires two real parameters. The second set of equations consists of  $(l - m)$  complex linear equations and thus requires  $2(l - m)$  additional real parameters. Thus, in this case,  $\text{codim}(\text{CPE}) = 2(l - m) + 2$ .

We summarize the codimension results as follows:

$$\text{codim}(\text{CPE}) = \begin{cases} 0 & \text{if } l < m, \\ 2(l - m) + 2 & \text{if } l \geq m. \end{cases} \quad (116)$$

These codimension results remain unchanged for the case  $\tilde{S} \in M_m^s$ . Note that in general  $\tilde{S} \notin M_m^s$  even for a reciprocal system with  $S \in M_n^s$ , unless  $\tilde{S}$  is a principal submatrix of  $S$ .

### C. Topology of a generic CPE point

For concreteness, we focus on the  $l = m$  case. The other cases will be discussed elsewhere. In the  $l = m$  case, coherent perfect extinction has a codimension of 2, thus one typically needs to adjust two real parameters to achieve it. Hence, we consider a system with an  $m \times m$  scattering submatrix  $\tilde{S}$  that depends on two parameters  $\tilde{\boldsymbol{\tau}} = (\tilde{\tau}_1, \tilde{\tau}_2) \in \tilde{\Omega}$ , where  $\tilde{\Omega}$  is a compact and simply connected subset of  $\mathbb{R}^2$ . The system is characterized by the map  $\tilde{S} : \tilde{\boldsymbol{\tau}} \in \tilde{\Omega} \mapsto \tilde{S}(\tilde{\boldsymbol{\tau}}) \in M_m$ . We assume that  $\tilde{S}$  is continuous. In the two-dimensional parameter space  $\tilde{\Omega}$ , coherent perfect extinction generically occurs at isolated points, referred to as *CPE points*. We must emphasize that a CPE point is generally not a CPA point, and vice versa, because the singular values of the submatrix  $\tilde{S}$  are generally different from those of the total matrix  $S$ . Without loss of generality, we assume that there is a unique generic CPE point  $\tilde{\boldsymbol{\tau}}_c = (\tilde{\tau}_{c1}, \tilde{\tau}_{c2}) \in \tilde{\Omega}$ , and there is no other point in  $\tilde{\Omega}$  where a pair of singular values of  $\tilde{S}$  coalesce or a singular value of  $\tilde{S}$  becomes zero. We introduce two simple closed curves in  $\tilde{\Omega}$ : a nontrivial loop  $\tilde{\boldsymbol{\gamma}}$  that encircles  $\tilde{\boldsymbol{\tau}}_c$  and a trivial loop  $\tilde{\boldsymbol{\gamma}}'$  that does not. Figure 8(b) shows a scheme of the parameter space [cf. Fig. 3(b)].

Now we study the topology of the  $\tilde{S}$  matrix near a generic CPE point. This problem is mathematically identical to that in Sec. IV C. We obtain the following topological results.

#### I. $\tilde{S} \in M_n$

Along a nontrivial loop  $\tilde{\boldsymbol{\gamma}}$ :

$$\text{wind}(\tilde{S}) = \tilde{\nu} = \pm 1, \quad \tilde{P} \equiv \frac{1}{2}. \quad (117)$$

Along a trivial loop  $\tilde{\boldsymbol{\gamma}}'$ :

$$\text{wind}(\tilde{S}) = \tilde{\nu} = 0, \quad \tilde{P} \equiv 0. \quad (118)$$

## 2. $\tilde{S} \in M_n^s$

We have additional results. Along a nontrivial loop  $\tilde{\gamma}$ :

$$\tilde{P}_m = \tilde{P}_{-m} \equiv \frac{1}{2}; \quad \tilde{P}_j \equiv 0, \quad j = \pm 1, \dots, \pm(m-1). \quad (119)$$

$$|\tilde{u}_m(2\pi)\rangle = -|\tilde{u}_m(0)\rangle; \quad |\tilde{u}_i(2\pi)\rangle = |\tilde{u}_i(0)\rangle, \quad i = 1, \dots, m-1. \quad (120)$$

Along a trivial loop  $\tilde{\gamma}'$ :

$$\tilde{P}_j \equiv 0, \quad j = \pm 1, \dots, \pm m. \quad (121)$$

$$|\tilde{u}_i(2\pi)\rangle = |\tilde{u}_i(0)\rangle, \quad i = 1, \dots, m. \quad (122)$$

### D. Effective two-band model

We apply the same method in Sec. IV D to construct an effective two-band model

$$\tilde{H}_{\text{eff}} = \sum_{i,j=1}^2 \tilde{\xi}_i \tilde{J}_{ij} s_j, \quad (123)$$

where  $\tilde{\xi} := \tilde{\tau} - \tilde{\tau}_c$  and  $\tilde{J} \in M_2(\mathbb{R})$ . We can show

$$2\tilde{P} \equiv \text{wind}(\tilde{S}) = \text{sgn}(\det \tilde{J}). \quad (124)$$

The effective two-band model in Eq. (123) remains unchanged for  $\tilde{S} \in M_n^s$ .

Thus our unified theory elucidates similar topological features of the two different effects of coherent perfect absorption and coherent perfect extinction (in the  $l = m$  case).

### E. Numerical demonstration

We demonstrate the topology of coherent perfect extinction with a concrete example. We highlight the similarities and differences between CPE and CPA.

The structure is modified from that in Ref. [103]. It consists of two layers [Fig. 9(a)]. The first layer is a photonic crystal slab with a lattice constant  $a$  and a thickness  $d = 0.5a$ . It contains a square array of air holes; each unit cell has a circular hole with a diameter  $d_c = 0.28a$  at the center and two elliptical holes with a major axis  $d_y = 0.56a$  and a minor axis  $d_x = 0.20a$  displaced by  $\pm\tilde{D} = \pm(0.375a, -0.18a)$  with respect to the center. The second layer is a uniform dielectric slab with a thickness  $d_s = 0.2a$ . Both slabs are made of materials with a scalar relative permittivity  $\varepsilon = \varepsilon_r + i\varepsilon_i$ , where  $\varepsilon_r = 8.0$  and  $\varepsilon_i \in [0, 0.01]$ .

The structure is illuminated by the light of both polarizations in the normal direction from the photonic crystal slab side. Here the electric fields of the  $p$  and  $s$  polarized light are aligned with the  $x$  and  $y$  directions, respectively [Fig. 9(a)].<sup>4</sup> The light frequency  $f = \omega/2\pi \in [1.1696, 1.17109]c/a$ . Since  $c/a < f < \sqrt{2}(c/a)$ , both the reflected light and the transmitted light have five diffraction

<sup>4</sup>Note that in Figs. 6(a) and 7(a), the  $p$  polarization is aligned with the  $-x$  direction, while in Fig. 9(a), it is aligned with the  $x$  direction. This is in accordance with the conventions adopted by the TMM [97] and RCWA [104] packages.

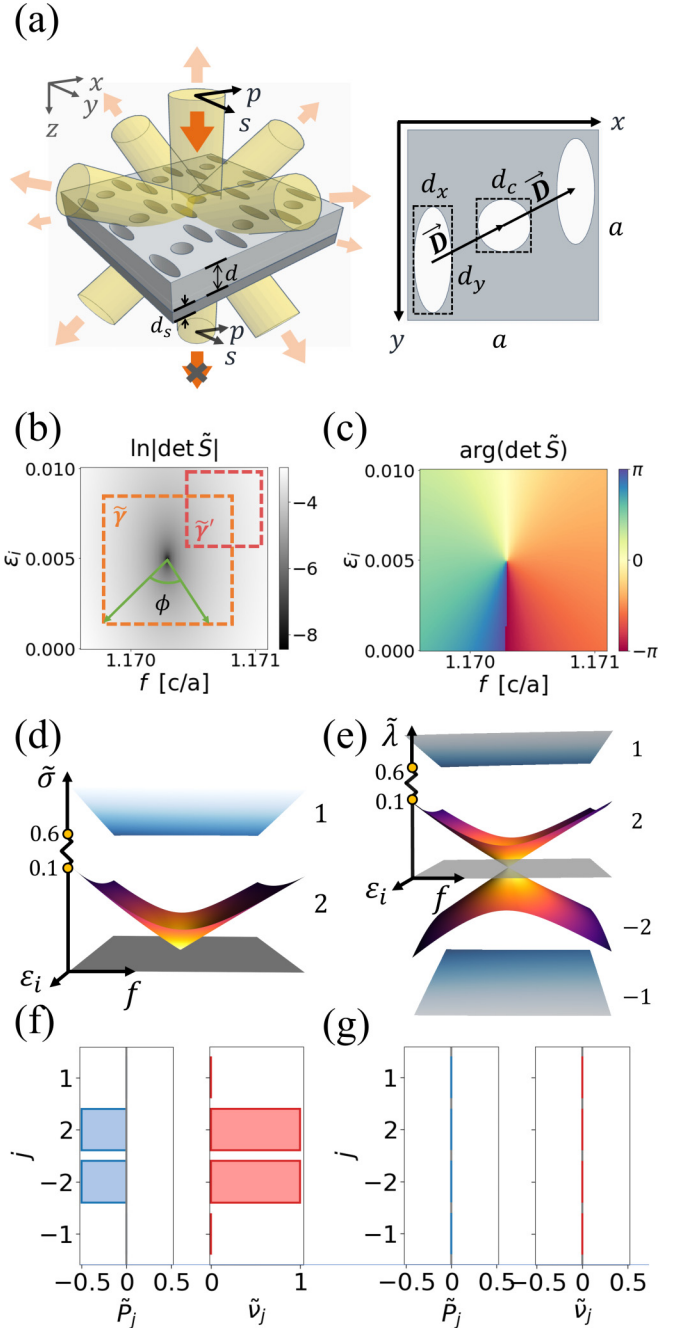


FIG. 9. A 20-port CPE system. (a) Left: structure. Right: unit cell. (b)  $\ln|\det \tilde{S}|(f, \varepsilon_i)$ . (c)  $\arg(\det \tilde{S})(f, \varepsilon_i)$ . (d)  $\tilde{\sigma}_i(f, \varepsilon_i)$ ,  $1 \leq i \leq 4$ . (e)  $\tilde{\lambda}_j(f, \varepsilon_i)$ ,  $j = \pm i$ . (f)  $\tilde{P}_j$  and  $\tilde{v}_j$  around  $\tilde{\gamma}$ . (g)  $\tilde{P}_j$  and  $\tilde{v}_j$  around  $\tilde{\gamma}'$ .

orders; each diffraction order has two polarizations. The total system is therefore characterized by a  $20 \times 20$  scattering matrix  $S \in M_{20}^s$ .

We focus on the direct transmission order and consider all the other diffraction orders as scattering loss. This is the conventional configuration for extinction measurement. The direct transmission is characterized by a  $2 \times 2$  submatrix of  $S$ :

$$\tilde{S}(f, \varepsilon_i) = \begin{pmatrix} t_{pp} & t_{ps} \\ t_{sp} & t_{ss} \end{pmatrix} \in M_2. \quad (125)$$

We calculate  $\tilde{S}(f, \varepsilon_i)$  using the rigorous coupled-wave analysis [104]. Figures 9(b) and 9(c) plot the logarithmic amplitude and phases of  $\det \tilde{S}$ , respectively. There is a single CPE point ( $f = 1.1703 c/a$ ,  $\varepsilon_i = 0.00495$ ) with a winding number

$$\text{wind}(\tilde{S}) = +1. \quad (126)$$

We introduce a nontrivial loop  $\tilde{\mathcal{Y}}(\phi)$  and a trivial loop  $\tilde{\mathcal{Y}}'(\phi)$  as illustrated in Fig. 9(b).

Figure 9(d) plots the singular values  $\tilde{\sigma}_1(f, \varepsilon_i)$  and  $\tilde{\sigma}_2(f, \varepsilon_i)$ .  $\tilde{\sigma}_2(f, \varepsilon_i)$  forms a half Dirac cone. From  $\tilde{S}$ , we construct  $\tilde{H}$  using the block matrix technique. Figure 9(e) plots the eigenvalues of  $\tilde{H}$ .  $\tilde{\lambda}_2(\tilde{H})$  and  $\tilde{\lambda}_{-2}(\tilde{H})$  form an upright Dirac cone.  $\tilde{S}$  is not a principal submatrix, thus  $\tilde{S} \notin M_2^s$  and does not have the Autonne-Takagi decomposition.

Figure 9(f) plots the polarization  $\tilde{P}_j$  and the skew polarization  $\tilde{v}_j$  around  $\tilde{\mathcal{Y}}$ . We observe that

$$\tilde{P}_2 = \tilde{P}_{-2} \approx \frac{1}{2}, \quad \tilde{P}_1 = \tilde{P}_{-1} \approx 0, \quad (127)$$

$$\tilde{v}_2 = \tilde{v}_{-2} \approx 1, \quad \tilde{v}_1 = \tilde{v}_{-1} \approx 0. \quad (128)$$

These observations may appear surprising at first sight given that  $\tilde{S} \notin M_n^s$ . The reason is that the loop  $\tilde{\mathcal{Y}}$  is sufficiently close to the CPE point, thus  $\tilde{H}$  is well described by the effective two-band model in Eq. (123), and the contributions from other bands are negligible. So these results confirm our discussions in Sec. IV D. The total polarization and skew polarization

$$\tilde{P} = \sum_{i=1}^2 \tilde{P}_i \equiv \frac{1}{2}, \quad \tilde{v} = \sum_{i=1}^2 \tilde{v}_i = 1, \quad (129)$$

which confirm Eq. (117).

Figure 9(g) plots the polarization  $\tilde{P}_j$  and the skew polarization  $\tilde{v}_j$  around  $\tilde{\mathcal{Y}}'$ . We observe that

$$\tilde{P}_j \approx 0, \quad \tilde{v}_j \approx 0, \quad \text{for all } j. \quad (130)$$

Again, these results arise because  $\tilde{\mathcal{Y}}'$  is sufficiently close to the CPE point. The total polarization and skew polarization

$$\tilde{P} = \sum_{i=1}^2 \tilde{P}_i \equiv 0, \quad \tilde{v} = \sum_{i=1}^2 \tilde{v}_i = 0, \quad (131)$$

which confirm Eq. (118).

### F. CPE for multichannel background-free sensing

We propose utilizing coherent perfect extinction for multichannel background-free sensing.

Detecting weak optical signals in the presence of strong backgrounds can be challenging for sensors, even if the same signals are detectable in the absence of background [105,106]. The bright background introduces proportionate noise that the weak signal must exceed to be observable [107,108]. Additionally, sensors must adjust their dynamic range to accommodate the background due to their finite bit depths, resulting in a coarser brightness scale that may render the signal indistinguishable from its background [107,108].

Coherent perfect extinction can overcome this problem for coherent light sources by removing all the background in multiple output channels prior to detection. This allows for

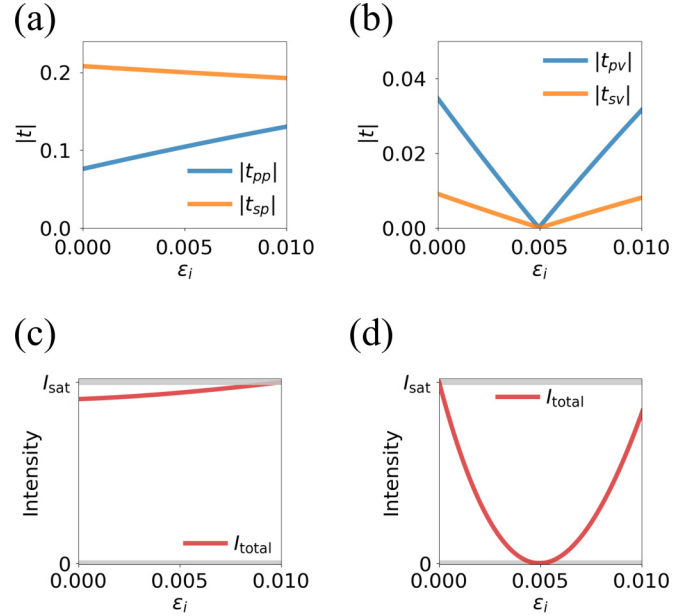


FIG. 10. CPE for multichannel background-free sensing. The device is as shown in Fig. 9. The unperturbed system is at the CPE point. If the incident light is  $p$ -polarized, the direct transmission exhibits nonzero background in both output polarizations (a), which limits the contrast of total intensity (c). If the incident light is  $v$ -polarized which leads to CPE, the direct transmission vanishes at the CPE point (b), resulting in significant contrast of total intensity (d). In (c) and (d), the input intensity is increased until one output channel reaches saturation.

maximal contrast when a signal arrives and full utilization of the detector's dynamic range.

We provide a proof-of-concept demonstration using the device in Fig. 9. We detect the imaginary part of the permittivity by measuring the direct transmission with both polarizations. Assuming the unperturbed system is at the CPE point, we perturb the imaginary part of the permittivity  $\varepsilon_i \in [0, 0.01]$ . If we select the incident light to be  $p$ -polarized, there is a bright background in both output polarizations [Fig. 10(a)], leading to limited contrast of total intensity under perturbation [Fig. 10(c)]. In contrast, if we select the incident polarization that leads to CPE (denoted as  $v$ -polarization), the background vanishes in both output polarizations [Fig. 10(b)], resulting in significant contrast of total intensity under perturbation [Fig. 10(d)]. This allows for full utilization of the detector's dynamic range by adjusting the incident light intensity.

## VI. DISCUSSION

We make three final remarks.

First, our analysis highlights the topological nature of CPA and CPE. This fact has both fundamental importance and practical applications. It reveals the robustness of these effects under generic parameter perturbations. It also provides useful criteria for localizing the occurrence of CPA and CPE in the parameter space, facilitating optical design to achieve these effects. For example, to find a CPA point in a two-dimensional parameter space, we can apply our topological theory and convert the 2D search problem into a series of 1D problems.

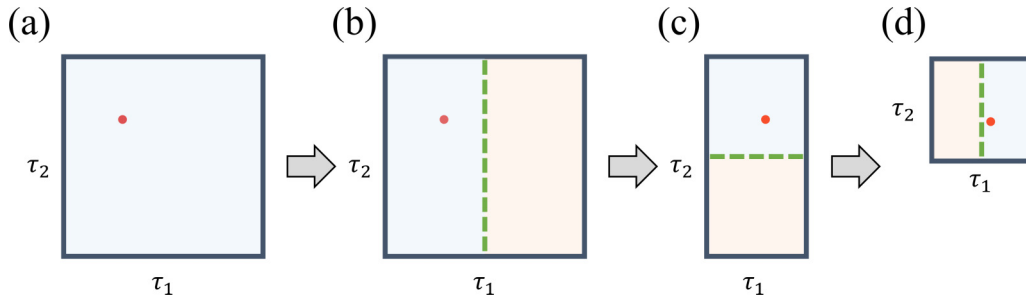


FIG. 11. Bisection search of a CPA point in a 2D parameter space. The red dot denotes the CPA point. The blue area denotes the search region. The green line segment bisects a search region. The orange area denotes the discarded region.

We first identify a simple loop along which the scattering matrix  $S$  exhibits a nonzero winding number [Fig. 11(a)]. Then the region enclosed by the loop must contain at least one CPA point. We can successively shrink the search region by bisecting it with a line segment [Fig. 11(b)]. If  $\det S = 0$  at any point along the line segment, that point is a CPA point. Otherwise,  $\det S$  must exhibit a nonzero winding number around the boundary of at least one of the two half-regions, which must contain a CPA point. We repeat this process until we localize a CPA point to the desired accuracy [Figs. 11(c) and 11(d)].

Second, our theory provides a general framework to investigate the singular topology of scattering matrices. It applies to any linear time-invariant systems described by scattering matrices [16], such as acoustic waves. It can be used to systematically investigate other topological phenomena in wave scattering beyond CPA and CPE.

Third, we have investigated the unique topological effects of reciprocal systems, which are not present in nonreciprocal systems. These effects arise due to the internal symmetry of reciprocity [15,86], which imposes direct constraints on the scattering matrix [109,110]. By applying a similar approach, we can explore the topological consequences of other symmetries on scattering matrices. We anticipate a rich set of symmetry-protected topological effects of scattering matrices.

## VII. CONCLUSION

In conclusion, we have presented a systematic theory on the singular topology of scattering matrices. We determine a set of topological characteristics for a general system and reveal unique topological features for a reciprocal system. We apply our theory to elucidate the topological nature of two physical phenomena: coherent perfect absorption and coherent perfect extinction, the latter being a new effect that accounts for both absorption and scattering losses. We propose utilizing coherent perfect extinction for multichannel background-free sensing. Our findings significantly advance our understanding of scattering phenomena and have important implications for the development of novel optical devices.

## ACKNOWLEDGMENTS

C.G. thanks A. Douglas Stone for pointing to Refs. [60,61]. This work is supported by a Simons Investigator in Physics grant from the Simons Foundation (Grant No. 827065).

## APPENDIX A: NOTATION

Here we summarize the mathematical notations used throughout this paper.  $\mathbb{Z}$ ,  $\mathbb{R}$ ,  $\mathbb{R}^*$ ,  $\mathbb{R}^+$ ,  $\mathbb{C}$  and  $\mathbb{C}^*$  denote the set of integers, real numbers, nonzero real numbers, positive real numbers, complex numbers, and nonzero complex numbers, respectively.  $M_n$ ,  $M_n^s$ , and  $U(n)$  denote the set of  $n \times n$  complex matrices, complex symmetric matrices, and unitary matrices, respectively. For  $M \in M_n$ ,  $M^T$ ,  $M^*$ , and  $M^\dagger$  denote the transpose, conjugate, and conjugate transpose of  $M$ , respectively.  $\mathbf{d}(M) = (d_1(M), \dots, d_n(M))^T$ ,  $\boldsymbol{\lambda}(M) = (\lambda_1(M), \dots, \lambda_n(M))^T$ , and  $\boldsymbol{\sigma}(M) = (\sigma_1(M), \dots, \sigma_n(M))^T$  denote the vector of diagonal elements, eigenvalues, and singular values of  $M$ , respectively. When describing the vectors of  $\mathbf{d}$ ,  $\boldsymbol{\lambda}$ , and  $\boldsymbol{\sigma}$ ,  $(M)$  may be omitted if there is no ambiguity.  $\|M\| := \sigma_{\max}(M)$  denotes the spectral norm of  $M$  [41].  $O$  and  $I$  denote  $n \times n$  zero and identity matrices, respectively;  $n$  should be clear from the context.  $\cong$  denotes isomorphism.  $a \equiv b \pmod{n}$  denotes  $a$  and  $b$  are congruent modulo  $n$ . In the special case when  $n = 1$ , we may write  $a \equiv b$  and omit  $\pmod{1}$ .

## APPENDIX B: FUNDAMENTAL GROUP OF $GL(n, \mathbb{C})$

Here we briefly outline the proof of Eq. (22):

$$\pi_1(GL(n, \mathbb{C})) \cong \mathbb{Z}. \quad (\text{B1})$$

Note that  $GL(n, \mathbb{C})$  is noncompact. Using polar decomposition, we can reduce the computation of  $\pi_1(GL(n, \mathbb{C}))$  to that of  $\pi_1(U(n))$ , where  $U(n)$  is the maximal compact subgroup of  $GL(n, \mathbb{C})$ . The fact that  $\pi_1(U(n)) \cong \mathbb{Z}$  completes the proof. The detailed proof can be found in Ref. [77], pp. 379, Sec. 13.3.

## APPENDIX C: PROOF OF RESULTS IN SEC. III A

Here we provide detailed proof of the results in Sec. III A, Eqs. (20), (21), (31), (35), and (36). The proof is based on the following theorem in matrix calculus:

*Theorem 1 (Jacobi's formula).* If  $A(t) \in M_n$  is invertible and differentiable in  $t \in \mathbb{R}$ , then

$$\frac{d}{dt} \det A(t) = [\det A(t)] \text{Tr} \left[ A(t)^{-1} \frac{d}{dt} A(t) \right]. \quad (\text{C1})$$

*Proof.* See Ref. [83], pp. 165, theorem 8.1. ■

**1. Proof of Eqs. (20) and (21)**

*Proof.* Eq. (20) is a direct result of Jacobi's formula:

$$\begin{aligned} \text{wind}(S) &:= \frac{1}{2\pi i} \int_0^{2\pi} \text{Tr} \left[ S^{-1} \frac{dS}{d\phi} \right] d\phi \\ &= \frac{1}{2\pi i} \int_0^{2\pi} \frac{1}{\det S} \frac{d \det S}{d\phi} d\phi =: \text{wind}(\det S). \end{aligned} \tag{C2}$$

Since  $\det(S)$  is continuous in the elements of  $S$  and  $S$  is continuous in  $\phi$ , we know that  $\det S(\phi)$  is a continuous function from  $[0, 2\pi]$  to  $\mathbb{C}$ . We have assumed that  $\det S(\phi) \neq 0$  and  $\det S(0) = \det S(2\pi)$ . So  $\det S(\phi)$  maps to a loop in the punctured plane  $\mathbb{C}^*$  and thus [76]

$$\text{wind}(\det S) \in \mathbb{Z}. \tag{C3}$$

This completes the proof of Eq. (21).

**2. Proof of Eq. (31)**

We first prove a general theorem that is useful in itself.

*Theorem 2.* Let  $H(\phi) \in M_n$  be Hermitian and differentiable with  $\phi \in [0, 2\pi]$  and  $H(0) = H(2\pi)$ . Suppose  $H(\phi)$  has distinct eigenvalues  $\lambda_i(\phi)$ ,  $i = 1, \dots, n$ . Denote the corresponding orthonormal eigenvectors  $|\psi_i(\phi)\rangle$ . Then the polarizations of all bands sum to 0 modulo 1:

$$\sum_{i=1}^n P_i := \frac{i}{2\pi} \sum_i \int_0^{2\pi} \langle \psi_i(\phi) | \frac{d}{d\phi} \psi_i(\phi) \rangle d\phi \equiv 0 \pmod{1}. \tag{C4}$$

*Proof.* We choose a gauge such that  $|\psi_i(\phi)\rangle$  is differentiable and  $|\psi_i(0)\rangle = |\psi_i(2\pi)\rangle$ . We introduce a matrix whose columns are  $|\psi_i(\phi)\rangle$ :

$$\Psi(\phi) := (|\psi_1(\phi)\rangle, |\psi_2(\phi)\rangle, \dots, |\psi_n(\phi)\rangle). \tag{C5}$$

Note that  $\Psi(\phi) \in U(n)$ ,  $\det \Psi(\phi)$  is differentiable, and  $|\det \Psi(\phi)| = 1 \neq 0$ . Therefore

$$\begin{aligned} \sum_{i=1}^n P_i &:= \frac{i}{2\pi} \sum_i \int_0^{2\pi} \langle \psi_i(\phi) | \frac{d}{d\phi} \psi_i(\phi) \rangle d\phi \\ &= \frac{i}{2\pi} \int_0^{2\pi} \text{Tr} \left[ \Psi^\dagger(\phi) \frac{d}{d\phi} \Psi(\phi) \right] d\phi \end{aligned} \tag{C6}$$

$$= -\text{wind}(\Psi) = -\text{wind}(\det \Psi) \in \mathbb{Z}. \tag{C7}$$

Since  $P_i$  is only defined by modulo 1, we should write

$$\sum_{i=1}^n P_i \equiv 0 \pmod{1}. \tag{C8}$$

This completes the proof. ■

Now we prove Eq. (31).

*Proof.* For a chiral symmetric Hermitian matrix  $H(\phi) \in M_{2n}$ , Eq. (29) shows  $P_i = P_{-i}$ , thus

$$P := \sum_{i=1}^n P_i = \sum_{i=1}^n P_{-i}. \tag{C9}$$

Theorem 2 requires that

$$2P = \sum_{i=1}^n (P_i + P_{-i}) \equiv 0 \pmod{1}, \tag{C10}$$

which is equivalent to

$$P \equiv 0, \quad \text{or} \quad P \equiv \frac{1}{2} \pmod{1}. \tag{C11}$$

This completes the proof of Eq. (31). ■

**3. Proof of Eq. (35)**

It suffices to prove that

$$\nu = \text{wind}(S). \tag{C12}$$

*Proof.* By assumption,  $S$  is a piecewise continuously differentiable function from  $[0, 2\pi]$  to  $M_n$  with  $S(0) = 2\pi$ . Also,  $\forall \phi \in [0, 2\pi]$ ,  $S(\phi)$  is invertible and has distinct singular values. Then  $S$  takes a continuous singular value decomposition:

$$S(\phi) = U(\phi)\Sigma(\phi)V^\dagger(\phi), \quad \phi \in [0, 2\pi], \tag{C13}$$

where  $U$ ,  $\Sigma$ , and  $V$  are as smooth as  $S$ . Moreover,

$$U(0) = U(2\pi), \quad \Sigma(0) = \Sigma(2\pi), \quad V(0) = V(2\pi). \tag{C14}$$

See Ref. [84], theorem 2.4 and 3.3(i) for proof of the existence of such a decomposition. Choosing such a decomposition corresponds to choosing a periodic gauge [6].

We use such a decomposition to prove Eq. (C12). On the one hand,

$$\text{wind}(S) := \frac{1}{2\pi i} \int_0^{2\pi} \text{Tr} \left[ S^{-1} \frac{dS}{d\phi} \right] d\phi \tag{C15}$$

$$= \frac{1}{2\pi i} \int_0^{2\pi} \text{Tr} \left[ V \Sigma^{-1} U^\dagger \frac{d(U \Sigma V^\dagger)}{d\phi} \right] d\phi \tag{C16}$$

$$\begin{aligned} &= \frac{1}{2\pi i} \int_0^{2\pi} \text{Tr} \left[ V \Sigma^{-1} U^\dagger \frac{dU}{d\phi} \Sigma V^\dagger \right. \\ &\quad \left. + V \Sigma^{-1} U^\dagger U \frac{d\Sigma}{d\phi} V^\dagger + V \Sigma^{-1} U^\dagger U \Sigma \frac{dV^\dagger}{d\phi} \right] d\phi \end{aligned} \tag{C17}$$

$$= \frac{1}{2\pi i} \int_0^{2\pi} \text{Tr} \left[ U^\dagger \frac{dU}{d\phi} + \Sigma^{-1} \frac{d\Sigma}{d\phi} + V \frac{dV^\dagger}{d\phi} \right] d\phi \tag{C18}$$

$$= \text{wind}(U) + \text{wind}(\Sigma) + \text{wind}(V^\dagger) \tag{C19}$$

$$= \text{wind}(U) - \text{wind}(V). \tag{C20}$$

To obtain Eq. (C19), we use Eq. (C14) and the fact that  $U$ ,  $\Sigma$  and  $V$  are invertible. To obtain Eq. (C20), we note that  $\det \Sigma \in \mathbb{R}^+$  thus

$$\text{wind}(\Sigma) = \text{wind}(\det \Sigma) = 0, \tag{C21}$$

and moreover,

$$\begin{aligned} \text{wind}(V^\dagger) &= \text{wind}(\det V^\dagger) = \text{wind}(\det V^{-1}) \\ &= -\text{wind}(\det V) = -\text{wind}(V). \end{aligned} \tag{C22}$$



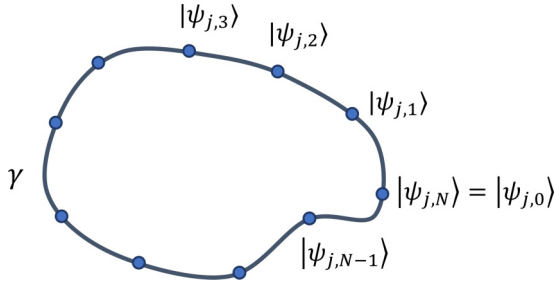


FIG. 12. Evolution of the eigenvector  $|\psi_j\rangle$  around a loop  $\gamma$  in the parameter space.

On the other hand,

$$v := \sum_{i=1}^n v_i = \frac{i}{\pi} \sum_i^n \int_0^{2\pi} \langle \Gamma \psi_i(\phi) | \frac{d}{d\phi} \psi_i(\phi) \rangle d\phi \quad (\text{C23})$$

$$= \frac{1}{2\pi i} \int_0^{2\pi} \sum_i^n \left( u_i^\dagger \frac{d}{d\phi} u_i - v_i^\dagger \frac{d}{d\phi} v_i \right) d\phi \quad (\text{C24})$$

$$= \frac{1}{2\pi i} \int_0^{2\pi} \text{Tr} \left[ U^\dagger \frac{dU}{d\phi} - V^\dagger \frac{dV}{d\phi} \right] d\phi \quad (\text{C25})$$

$$= \text{wind}(U) - \text{wind}(V). \quad (\text{C26})$$

To obtain Eq. (C24), we use Eqs. (9) and (13). To obtain Eq. (C25), we use the fact that  $u_i$  and  $v_i$  are the  $i$ th columns of  $U$  and  $V$ , respectively. Comparing Eqs. (C20) and (C26), we obtain Eq. (C12) and complete the proof. ■

#### 4. Proof of Eq. (36)

*Proof.* As in the proof above, we choose a periodic gauge. Then

$$P := \sum_{i=1}^n P_i = \frac{i}{2\pi} \sum_i^n \int_0^{2\pi} \langle \psi_i(\phi) | \frac{d}{d\phi} \psi_i(\phi) \rangle d\phi \quad (\text{C27})$$

$$= \frac{i}{4\pi} \int_0^{2\pi} \sum_i^n \left( u_i^\dagger \frac{d}{d\phi} u_i + v_i^\dagger \frac{d}{d\phi} v_i \right) d\phi \quad (\text{C28})$$

$$= -\frac{1}{4\pi i} \int_0^{2\pi} \text{Tr} \left[ U^\dagger \frac{dU}{d\phi} + V^\dagger \frac{dV}{d\phi} \right] d\phi \quad (\text{C29})$$

$$= -\frac{1}{2} [\text{wind}(U) + \text{wind}(V)]. \quad (\text{C30})$$

Combining Eqs. (C26) and (C30), we obtain

$$v - 2P = 2 \text{wind}(U) \in 2\mathbb{Z}. \quad (\text{C31})$$

Since  $P$  is only defined by modulo 1, we should write

$$2P \equiv v \pmod{2}, \quad (\text{C32})$$

which is equivalent to Eq. (36). This completes the proof. ■

#### APPENDIX D: PROOF OF EQ. (46)

Here we prove Eq. (46). For convenience, we introduce an alternative definition of polarization  $P_j$  with a discrete formulation.

As shown in Fig. 12, we choose  $N$  representative eigenvectors  $|\psi_{j,0}\rangle$  to  $|\psi_{j,N-1}\rangle$  around the loop  $\gamma$ , where

$$|\psi_{j,k}\rangle \equiv \left| \psi_j \left( \phi = \frac{k}{N} 2\pi \right) \right\rangle, \quad j = \pm 1, \dots, \pm n, \quad k = 0, \dots, N-1. \quad (\text{D1})$$

Note that  $|\psi_{j,N}\rangle = |\psi_{j,0}\rangle$ . Then we define the polarization  $P_j$  by

$$P_j := -\frac{1}{2\pi} \lim_{N \rightarrow \infty} \text{Im} \ln W_{j,N}, \quad (\text{D2})$$

where

$$W_{j,N} := \langle \psi_{j,0} | \psi_{j,1} \rangle \langle \psi_{j,1} | \psi_{j,2} \rangle \dots \langle \psi_{j,N-1} | \psi_{j,0} \rangle \in \mathbb{C}^*. \quad (\text{D3})$$

One can prove that Eq. (D2) is equivalent to Eq. (25) [6].

For a reciprocal system, the eigenvectors of  $H$  are given in Eq. (45) as reproduced below:

$$|\psi_i\rangle = \frac{1}{\sqrt{2}} e^{i\alpha_i} \begin{pmatrix} u_i^* \\ u_i \end{pmatrix}, \quad |\psi_{-i}\rangle = \frac{1}{\sqrt{2}} e^{i\alpha_{-i}} \begin{pmatrix} u_i^* \\ -u_i \end{pmatrix}. \quad (\text{D4})$$

Then, for any given  $j = \pm 1, \dots, \pm n$ ,

$$\begin{aligned} W_{j,N} &= \langle \psi_{j,0} | \psi_{j,1} \rangle \langle \psi_{j,1} | \psi_{j,2} \rangle \dots \langle \psi_{j,N-1} | \psi_{j,0} \rangle \\ &= \langle \psi_{j,0}^* | \psi_{j,1}^* \rangle \langle \psi_{j,1}^* | \psi_{j,2}^* \rangle \dots \langle \psi_{j,N-1}^* | \psi_{j,0}^* \rangle \\ &= W_{j,N}^* \end{aligned} \quad (\text{D5})$$

Therefore  $W_{j,N} \in \mathbb{R}^*$ , and thus we obtain Eq. (46)

$$P_j \in \frac{1}{2} \mathbb{Z}_2. \quad (\text{D6})$$

This completes the proof.

#### APPENDIX E: PROOF OF RESULTS IN SEC. IV C

Here we provide detailed proof of the results in Sec. IV C, Eqs. (54)–(59).

##### 1. Proof of Eqs. (57) and (59)

The proofs of Eqs. (57) and (59) can be found in Ref. [78], theorem 2.6.

##### 2. Proof of Eqs. (54) and (55)

Considering Eqs. (35) and (36), it suffices to prove

$$\begin{aligned} \text{wind}(S) &= \pm 1 \quad \text{along a nontrivial loop } \gamma, \\ \text{wind}(S) &= 0 \quad \text{along a trivial loop } \gamma'. \end{aligned} \quad (\text{E1})$$

*Proof.* We use the fact that the winding number is homotopy invariant [76]. By our assumptions,  $\tau_c$  is the single generic zero point of  $\det S(\tau)$  in  $\Omega$  (Fig. 13). The trivial loop  $\gamma'$  can be shrunk to a point with  $\det S \neq 0$  by homotopy, therefore

$$\text{wind}(S) = \text{wind}(\det S) = 0 \quad \text{along } \gamma'. \quad (\text{E2})$$

Instead, the nontrivial loop  $\gamma$  can only be shrunk to a small circle  $\gamma_c$  around  $\tau_c$  by homotopy. We take the first-order expansion of  $\det S(\tau)$  in  $\gamma_c$ :

$$\det S(\tau_c + \xi) = z_1 \xi_1 + z_2 \xi_2 + O(\xi^2) \quad (\text{E3})$$

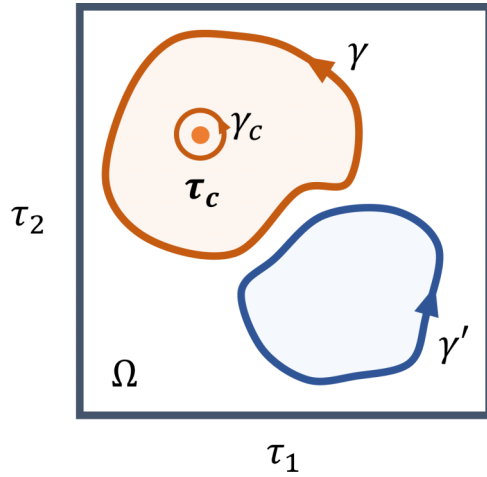


FIG. 13. Scheme of parameter space.  $\gamma$  is homotopic to  $\gamma_c$ .  $\gamma'$  can be shrunk to a point.

where  $z_1, z_2 \in \mathbb{C}$ . Generically,  $z_1$  and  $z_2$  are nonzero and linearly independent over  $\mathbb{R}$ . We can rewrite Eq. (E3) as

$$\begin{pmatrix} \text{Re det } S(\tau_c + \xi) \\ \text{Im det } S(\tau_c + \xi) \end{pmatrix} \approx \begin{pmatrix} z_{1r} & z_{2r} \\ z_{1i} & z_{2i} \end{pmatrix} \begin{pmatrix} \xi_1 \\ \xi_2 \end{pmatrix} = Z \begin{pmatrix} \xi_1 \\ \xi_2 \end{pmatrix}. \quad (\text{E4})$$

Direct calculation shows that

$$\text{wind}(S) = \text{sgn}(\det Z) = \pm 1 \quad \text{along } \gamma_c. \quad (\text{E5})$$

Since  $\det S$  is homotopy invariant,

$$\text{wind}(S) = \pm 1 \quad \text{along } \gamma. \quad (\text{E6})$$

This completes the proof.  $\blacksquare$

### 3. Proof of Eqs. (56) and (58)

*Proof.* For a reciprocal system, we can choose the eigenvectors  $|\psi_j\rangle$  of  $H$  as given in Eq. (D4). Such a choice corresponds to choosing a parallel-transport gauge [6], since

$$\begin{aligned} A_j(\phi) &= -\text{Im} \langle \psi_j(\phi) | \partial_\phi \psi_j(\phi) \rangle \\ &= -\text{Im Re} \langle u_{|j|}(\phi) | \partial_\phi u_{|j|}(\phi) \rangle = 0. \end{aligned} \quad (\text{E7})$$

In such a gauge, the Berry phase is just the phase mismatch at the end of the loop [6]:

$$P_j \equiv -\frac{1}{2\pi} \text{Im} \ln \text{Re} \langle u_{|j|}(2\pi) | u_{|j|}(0) \rangle. \quad (\text{E8})$$

Along a nontrivial loop  $\gamma$ , we substitute Eq. (57) into Eq. (E8) and obtain Eq. (56):

$$P_j \equiv \begin{cases} \frac{1}{2}, & j = \pm n, \\ 0, & j = \pm 1, \pm 2, \dots, \pm(n-1). \end{cases} \quad (\text{E9})$$

Along a trivial loop  $\gamma'$ , we substitute Eq. (59) into Eq. (E8) and obtain Eq. (58):

$$P_j \equiv 0, \quad j = \pm 1, \pm 2, \dots, \pm n. \quad (\text{E10})$$

This completes the proof.  $\blacksquare$

### APPENDIX F: BASIS CONVENTION

This paper adopts the standard basis convention where the output mode is the time reversal of the input mode. This results in a symmetric scattering matrix for reciprocal systems, which is useful for our purpose. Our convention differs from the basis convention that is commonly used in the transfer matrix method (TMM). Here, we provide a detailed discussion of these two conventions.

Figure 14(a) shows the convention commonly used in TMM [97]. Note that when the light propagation direction is reversed, the direction of  $p$  polarization is flipped, while the direction of  $s$  polarization is preserved. Under this convention, the scattering matrix takes the form

$$\tilde{S} = \begin{pmatrix} \tilde{r}_{ss}^F & \tilde{r}_{sp}^F & \tilde{t}_{ss}^B & \tilde{t}_{sp}^B \\ \tilde{r}_{ps}^F & \tilde{r}_{pp}^F & \tilde{t}_{ps}^B & \tilde{t}_{pp}^B \\ \tilde{t}_{ss}^F & \tilde{t}_{sp}^F & \tilde{r}_{ss}^B & \tilde{r}_{sp}^B \\ \tilde{t}_{ps}^F & \tilde{t}_{pp}^F & \tilde{r}_{ps}^B & \tilde{r}_{pp}^B \end{pmatrix}. \quad (\text{F1})$$

Figure 14(b) shows the convention we adopt [15]. Note that when the light propagation direction is reversed, the electric field directions of both  $s$  and  $p$  polarizations are preserved.

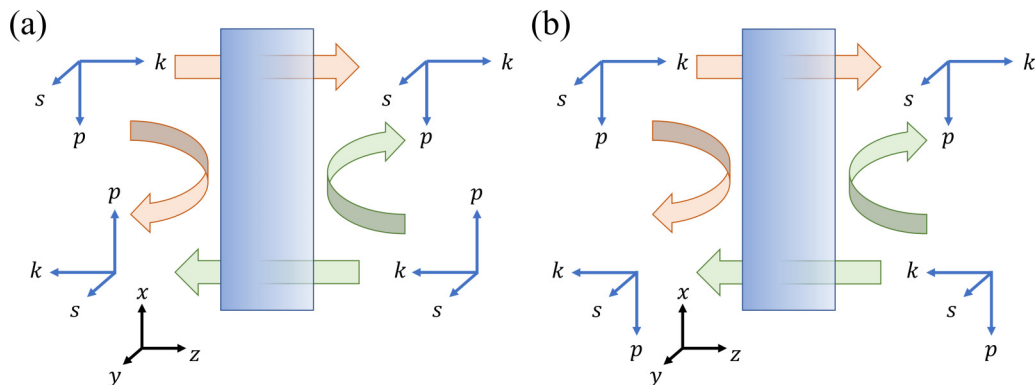


FIG. 14. Basis conventions. (a) Transfer matrix method convention. (b) Time reversal convention.

Under this convention, the scattering matrix takes the form

$$S = \begin{pmatrix} r_{ss}^F & r_{sp}^F & t_{ss}^B & t_{sp}^B \\ r_{ps}^F & r_{pp}^F & t_{ps}^B & t_{pp}^B \\ t_{ss}^F & t_{sp}^F & r_{ss}^B & r_{sp}^B \\ t_{ps}^F & t_{pp}^F & r_{ps}^B & r_{pp}^B \end{pmatrix} = \begin{pmatrix} \tilde{r}_{ss}^F & \tilde{r}_{sp}^F & \tilde{t}_{ss}^B & -\tilde{t}_{sp}^B \\ -\tilde{r}_{ps}^F & -\tilde{r}_{pp}^F & -\tilde{t}_{ps}^B & \tilde{t}_{pp}^B \\ \tilde{t}_{ss}^F & \tilde{t}_{sp}^F & \tilde{r}_{ss}^B & -\tilde{r}_{sp}^B \\ \tilde{t}_{ps}^F & \tilde{t}_{pp}^F & \tilde{r}_{ps}^B & -\tilde{r}_{pp}^B \end{pmatrix}. \quad (\text{F2})$$

We note that for a generic reciprocal system,

$$S = S^T, \quad \tilde{S} \neq \tilde{S}^T. \quad (\text{F3})$$

This highlights the importance of the basis convention on the  $S$ -matrix representation.

- 
- [1] C. Nash and S. Sen, *Topology and Geometry for Physicists*, Dover Books on Mathematics (Dover Publications, Mineola, N.Y., 2011).
- [2] M. Nakahara, *Geometry, Topology, and Physics*, 2nd ed., Graduate Student Series in Physics (Institute of Physics Publishing, Bristol; Philadelphia, 2003).
- [3] H. Eschrig, *Topology and Geometry for Physicists*, Lecture Notes in Physics Vol. 822 (Springer, Heidelberg, New York, 2011).
- [4] C. N. Yang, M. L. Ge, and Y.-H. He, *Topology and Physics* (World Scientific, New Jersey, 2018).
- [5] F. D. M. Haldane, Nobel Lecture: Topological quantum matter, *Rev. Mod. Phys.* **89**, 040502 (2017).
- [6] D. Vanderbilt, *Berry Phases in Electronic Structure Theory* (Cambridge University Press, Cambridge, 2018).
- [7] D. J. Thouless, M. Kohmoto, M. P. Nightingale, and M. den Nijs, Quantized Hall conductance in a two-dimensional periodic potential, *Phys. Rev. Lett.* **49**, 405 (1982).
- [8] M. V. Berry, Quantal phase factors accompanying adiabatic changes, *Proc. R. Soc. London A* **392**, 45 (1984).
- [9] J. Zak, Berry's phase for energy bands in solids, *Phys. Rev. Lett.* **62**, 2747 (1989).
- [10] F. D. M. Haldane, Model for a quantum Hall effect without Landau levels: Condensed-matter realization of the "parity anomaly", *Phys. Rev. Lett.* **61**, 2015 (1988).
- [11] C. L. Kane and E. J. Mele,  $Z_2$  Topological order and the quantum spin Hall effect, *Phys. Rev. Lett.* **95**, 146802 (2005).
- [12] M. König, S. Wiedmann, C. Brüne, A. Roth, H. Buhmann, L. W. Molenkamp, X.-L. Qi, and S.-C. Zhang, Quantum spin Hall insulator state in HgTe quantum wells, *Science* **318**, 766 (2007).
- [13] M. Reed and B. Simon, *Methods of Modern Mathematical Physics. 3: Scattering Theory*, (Academic Press, New York, 2003).
- [14] S. Datta, *Electronic Transport in Mesoscopic Systems*, 1st ed. (Cambridge University Press, 1995).
- [15] H. A. Haus, *Waves and Fields in Optoelectronics* (Prentice-Hall, Englewood Cliffs, NJ, 1984).
- [16] P. Sheng, *Introduction to Wave Scattering, Localization, and Mesoscopic Phenomena*, 2nd ed., Springer Series in Materials Science Vol. 88 (Springer, Berlin; New York, 2006).
- [17] J. R. Taylor, *Scattering Theory: The Quantum Theory of Nonrelativistic Collisions* (Dover Publications, Mineola, NY, 2006).
- [18] J. F. Nye and M. V. Berry, Dislocations in wave trains, *Proc. R. Soc. London A* **336**, 165 (1974).
- [19] T. Bauer, P. Banzer, E. Karimi, S. Orlov, A. Rubano, L. Marrucci, E. Santamato, R. W. Boyd, and G. Leuchs, Observation of optical polarization Möbius strips, *Science* **347**, 964 (2015).
- [20] Y. Zhang, A. Chen, W. Liu, C. W. Hsu, B. Wang, F. Guan, X. Liu, L. Shi, L. Lu, and J. Zi, Observation of polarization vortices in momentum space, *Phys. Rev. Lett.* **120**, 186103 (2018).
- [21] B. Wang, W. Liu, M. Zhao, J. Wang, Y. Zhang, A. Chen, F. Guan, X. Liu, L. Shi, and J. Zi, Generating optical vortex beams by momentum-space polarization vortices centred at bound states in the continuum, *Nat. Photonics* **14**, 623 (2020).
- [22] C. Wang, W. R. Sweeney, A. D. Stone, and L. Yang, Coherent perfect absorption at an exceptional point, *Science* **373**, 1261 (2021).
- [23] C. Guo, M. Xiao, M. Orenstein, and S. Fan, Structured 3D linear space-time light bullets by nonlocal nanophotonics, *Light Sci. Appl.* **10**, 160 (2021).
- [24] D. Kim, A. Baucour, Y.-S. Choi, J. Shin, and M.-K. Seo, Spontaneous generation and active manipulation of real-space optical vortices, *Nature (London)* **611**, 48 (2022).
- [25] Y. Guo, M. Xiao, and S. Fan, Topologically protected complete polarization conversion, *Phys. Rev. Lett.* **119**, 167401 (2017).
- [26] Y. Guo, M. Xiao, Y. Zhou, and S. Fan, Arbitrary polarization conversion with a photonic crystal slab, *Adv. Opt. Mater.* **7**, 1801453 (2019).
- [27] C. Guo, M. Xiao, Y. Guo, L. Yuan, and S. Fan, Meron spin textures in momentum space, *Phys. Rev. Lett.* **124**, 106103 (2020).
- [28] Y. Zeng, G. Hu, K. Liu, Z. Tang, and C.-W. Qiu, Dynamics of topological polarization singularity in momentum space, *Phys. Rev. Lett.* **127**, 176101 (2021).
- [29] W. Liu, W. Liu, L. Shi, and Y. Kivshar, Topological polarization singularities in metaphotonics, *Nanophotonics* **10**, 1469 (2021).
- [30] M. Kang, Z. Zhang, T. Wu, X. Zhang, Q. Xu, A. Krasnok, J. Han, and A. Alù, Coherent full polarization control based on bound states in the continuum, *Nat. Commun.* **13**, 4536 (2022).
- [31] T. Zhu, C. Guo, J. Huang, H. Wang, M. Orenstein, Z. Ruan, and S. Fan, Topological optical differentiator, *Nat. Commun.* **12**, 680 (2021).

- [32] O. Y. Long, C. Guo, H. Wang, and S. Fan, Isotropic topological second-order spatial differentiator operating in transmission mode, *Opt. Lett.* **46**, 3247 (2021).
- [33] Y. Huang, Y. Shen, C. Min, S. Fan, and G. Veronis, Unidirectional reflectionless light propagation at exceptional points, *Nanophotonics* **6**, 977 (2017).
- [34] Q. Song, M. Odeh, J. Zúñiga-Pérez, B. Kanté, and P. Genevet, Plasmonic topological metasurface by encircling an exceptional point, *Science* **373**, 1133 (2021).
- [35] A. Krasnok, D. Baranov, H. Li, M.-A. Miri, F. Monticone, and A. Alù, Anomalies in light scattering, *Adv. Opt. Photon.* **11**, 892 (2019).
- [36] X. Ni, S. Yves, A. Krasnok, and A. Alù, Topological Metamaterials, *Chem. Rev.* **123**, 7585 (2023).
- [37] I. C. Fulga, F. Hassler, A. R. Akhmerov, and C. W. J. Beenakker, Scattering formula for the topological quantum number of a disordered multimode wire, *Phys. Rev. B* **83**, 155429 (2011).
- [38] I. C. Fulga, F. Hassler, and A. R. Akhmerov, Scattering theory of topological insulators and superconductors, *Phys. Rev. B* **85**, 165409 (2012).
- [39] S. Franca, F. Hassler, and I. C. Fulga, Topological reflection matrix, *Phys. Rev. B* **105**, 155121 (2022).
- [40] S. Franca, V. Könye, F. Hassler, J. van den Brink, and C. Fulga, Non-hermitian physics without gain or loss: the skin effect of reflected waves, *Phys. Rev. Lett.* **129**, 086601 (2022).
- [41] R. A. Horn and C. R. Johnson, *Matrix Analysis*, 2nd ed. (Cambridge University Press, New York, NY, 2017).
- [42] D. A. B. Miller, Waves, modes, communications, and optics: A tutorial, *Adv. Opt. Photon.* **11**, 679 (2019).
- [43] C. Guo and S. Fan, Reciprocity constraints on reflection, *Phys. Rev. Lett.* **128**, 256101 (2022).
- [44] D. A. B. Miller, L. Zhu, and S. Fan, Universal modal radiation laws for all thermal emitters, *Proc. Natl. Acad. Sci. USA* **114**, 4336 (2017).
- [45] C. Guo and S. Fan, Majorization theory for unitary control of optical absorption and emission, *Phys. Rev. Lett.* **130**, 146202 (2023).
- [46] S. M. Popoff, G. Lerosey, R. Carminati, M. Fink, A. C. Boccara, and S. Gigan, Measuring the transmission matrix in optics: an approach to the study and control of light propagation in disordered media, *Phys. Rev. Lett.* **104**, 100601 (2010).
- [47] S. Rotter and S. Gigan, Light fields in complex media: Mesoscopic scattering meets wave control, *Rev. Mod. Phys.* **89**, 015005 (2017).
- [48] D. A. B. Miller, Self-configuring universal linear optical component [Invited], *Photon. Res.* **1**, 1 (2013).
- [49] J. Carolan, C. Harrold, C. Sparrow, E. Martín-López, N. J. Russell, J. W. Silverstone, P. J. Shadbolt, N. Matsuda, M. Oguma, M. Itoh, G. D. Marshall, M. G. Thompson, J. C. F. Matthews, T. Hashimoto, J. L. O'Brien, and A. Laing, Universal linear optics, *Science* **349**, 711 (2015).
- [50] Y. Shen, N. C. Harris, S. Skirlo, M. Prabhu, T. Baehr-Jones, M. Hochberg, X. Sun, S. Zhao, H. Larochelle, D. Englund, and M. Soljačić, Deep learning with coherent nanophotonic circuits, *Nat. Photonics* **11**, 441 (2017).
- [51] Y. D. Chong, L. Ge, H. Cao, and A. D. Stone, Coherent perfect absorbers: Time-reversed lasers, *Phys. Rev. Lett.* **105**, 053901 (2010).
- [52] W. Wan, Y. Chong, L. Ge, H. Noh, A. D. Stone, and H. Cao, Time-reversed lasing and interferometric control of absorption, *Science* **331**, 889 (2011).
- [53] Y. Sun, W. Tan, H.-q. Li, J. Li, and H. Chen, Experimental demonstration of a coherent perfect absorber with PT phase transition, *Phys. Rev. Lett.* **112**, 143903 (2014).
- [54] D. G. Baranov, A. Krasnok, T. Shegai, A. Alù, and Y. Chong, Coherent perfect absorbers: Linear control of light with light, *Nat. Rev. Mater.* **2**, 17064 (2017).
- [55] A. Müllers, B. Santra, C. Baals, C. Baals, J. Jiang, J. Benary, R. Labouvie, D. A. Zezyulin, V. V. Konotop, and H. Ott, Coherent perfect absorption of nonlinear matter waves, *Sci. Adv.* **4**, eaat6539 (2018).
- [56] K. Pichler, M. Kühmayer, J. Böhm, A. Brandstötter, P. Ambichl, U. Kuhl, and S. Rotter, Random anti-lasing through coherent perfect absorption in a disordered medium, *Nature (London)* **567**, 351 (2019).
- [57] W. R. Sweeney, C. W. Hsu, S. Rotter, and A. D. Stone, Perfectly absorbing exceptional points and chiral absorbers, *Phys. Rev. Lett.* **122**, 093901 (2019).
- [58] L. Chen, T. Kottos, and S. M. Anlage, Perfect absorption in complex scattering systems with or without hidden symmetries, *Nat. Commun.* **11**, 5826 (2020).
- [59] Y. Slobodkin, G. Weinberg, H. Hörner, K. Pichler, S. Rotter, and O. Katz, Massively degenerate coherent perfect absorber for arbitrary wavefronts, *Science* **377**, 995 (2022).
- [60] W. R. Sweeney, C. W. Hsu, and A. D. Stone, Theory of reflectionless scattering modes, *Phys. Rev. A* **102**, 063511 (2020).
- [61] A. D. Stone, W. R. Sweeney, C. W. Hsu, K. Wisal, and Z. Wang, Reflectionless excitation of arbitrary photonic structures: A general theory, *Nanophotonics* **10**, 343 (2021).
- [62] M. Horodyski, M. Kühmayer, C. Ferise, S. Rotter, and M. Davy, Anti-reflection structure for perfect transmission through complex media, *Nature (London)* **607**, 281 (2022).
- [63] T. Kitagawa, E. Berg, M. Rudner, and E. Demler, Topological characterization of periodically driven quantum systems, *Phys. Rev. B* **82**, 235114 (2010).
- [64] L. Herviou, J. H. Bardarson, and N. Regnault, Defining a bulk-edge correspondence for non-Hermitian Hamiltonians via singular-value decomposition, *Phys. Rev. A* **99**, 052118 (2019).
- [65] L. Herviou, N. Regnault, and J. H. Bardarson, Entanglement spectrum and symmetries in non-Hermitian fermionic non-interacting models, *SciPost Phys.* **7**, 069 (2019).
- [66] D. Porras and S. Fernández-Lorenzo, Topological amplification in photonic lattices, *Phys. Rev. Lett.* **122**, 143901 (2019).
- [67] E. J. Bergholtz, J. C. Budich, and F. K. Kunst, Exceptional topology of non-Hermitian systems, *Rev. Mod. Phys.* **93**, 015005 (2021).
- [68] D. A. B. Miller, All linear optical devices are mode converters, *Opt. Express* **20**, 23985 (2012).
- [69] G. W. Stewart and J. Sun, *Matrix Perturbation Theory* (Academic Press, Boston, 1990).
- [70] R. A. Horn and C. R. Johnson, *Topics in Matrix Analysis* (Cambridge University Press, Cambridge, 2008).
- [71] Z. Gong, Y. Ashida, K. Kawabata, K. Takasan, S. Higashikawa, and M. Ueda, Topological phases of non-Hermitian systems, *Phys. Rev. X* **8**, 031079 (2018).

- [72] C.-K. Chiu, J. C. Y. Teo, A. P. Schnyder, and S. Ryu, Classification of topological quantum matter with symmetries, *Rev. Mod. Phys.* **88**, 035005 (2016).
- [73] J. K. Asbóth, L. Oroszlány, and A. Pályi, *A Short Course on Topological Insulators: Band Structure and Edge States in One and Two Dimensions* (Springer, Cham, 2016).
- [74] X. Chen, Z.-C. Gu, Z.-X. Liu, and X.-G. Wen, Symmetry protected topological orders and the group cohomology of their symmetry group, *Phys. Rev. B* **87**, 155114 (2013).
- [75] J. D. Achenbach, *Reciprocity in Elastodynamics* (Cambridge University Press, Cambridge, 2004).
- [76] J. Roe, *Winding around: The Winding Number in Topology, Geometry, and Analysis* (American Mathematical Society, Providence, Rhode Island, 2015).
- [77] B. C. Hall, *Lie Groups, Lie Algebras, and Representations: An Elementary Introduction*, 2nd ed. (Springer, Cham, 2015).
- [78] L. Dieci, A. Papini, and A. Pugliese, Takagi factorization of matrices depending on parameters and locating degeneracies of singular values, *SIAM J. Matrix Anal. Appl.* **43**, 1148 (2022).
- [79] I. Mondragon-Shem, T. L. Hughes, J. Song, and E. Prodan, Topological criticality in the chiral-symmetric AIII class at strong disorder, *Phys. Rev. Lett.* **113**, 046802 (2014).
- [80] J. Song and E. Prodan, AIII and BDI topological systems at strong disorder, *Phys. Rev. B* **89**, 224203 (2014).
- [81] R. L. Graham, D. E. Knuth, and O. Patashnik, *Concrete Mathematics: A Foundation for Computer Science*, 2nd ed. (Addison-Wesley, Reading, Massachusetts, 1994).
- [82] M. Maffei, A. Dauphin, F. Cardano, M. Lewenstein, and P. Massignan, Topological characterization of chiral models through their long time dynamics, *New J. Phys.* **20**, 013023 (2018).
- [83] J. R. Magnus and H. Neudecker, *Matrix Differential Calculus with Applications in Statistics and Econometrics*, 3rd ed. (Wiley, Hoboken, NJ, 2019).
- [84] J.-L. Chern and L. Dieci, Smoothness and periodicity of some matrix decompositions, *SIAM J. Matrix Anal. Appl.* **22**, 772 (2001).
- [85] Z. Zhao, C. Guo, and S. Fan, Connection of temporal coupled-mode-theory formalisms for a resonant optical system and its time-reversal conjugate, *Phys. Rev. A* **99**, 033839 (2019).
- [86] C. Guo, Z. Zhao, and S. Fan, Internal transformations and internal symmetries in linear photonic systems, *Phys. Rev. A* **105**, 023509 (2022).
- [87] L. Autonne, *Sur les matrices hypohermitiennes et sur les matrices unitaires*, Vol. 38 (A. Rey, 1915).
- [88] T. Takagi, On an algebraic problem related to an analytic theorem of Carathéodory and Fejér and on an allied theorem of Landau, *Jpn. J. Math.: Trans. Abstr.* **1**, 83 (1924).
- [89] T. Kato, *Perturbation Theory for Linear Operators*, Classics in Mathematics (Springer, Berlin, 1995).
- [90] P.-O. Löwdin, A note on the quantum-mechanical perturbation theory, *J. Chem. Phys.* **19**, 1396 (1951).
- [91] A. Messiah, *Quantum Mechanics* (Dover Publications, Inc, Garden City, New York, 1999).
- [92] D. J. Klein, Degenerate perturbation theory, *J. Chem. Phys.* **61**, 786 (1974).
- [93] K. Suzuki and R. Okamoto, Degenerate perturbation theory in quantum mechanics, *Prog. Theor. Phys.* **70**, 439 (1983).
- [94] G. P. Mikitik and Y. V. Sharlai, Manifestation of Berry's phase in metal physics, *Phys. Rev. Lett.* **82**, 2147 (1999).
- [95] Y. Zhang, Y.-W. Tan, H. L. Stormer, and P. Kim, Experimental observation of the quantum Hall effect and Berry's phase in graphene, *Nature (London)* **438**, 201 (2005).
- [96] D. Xiao, M.-C. Chang, and Q. Niu, Berry phase effects on electronic properties, *Rev. Mod. Phys.* **82**, 1959 (2010).
- [97] T. G. Mackay and A. Lakhtakia, *The Transfer-Matrix Method in Electromagnetics and Optics* (Springer, Cham, 2020).
- [98] C. F. Bohren and D. R. Huffman, *Absorption and Scattering of Light by Small Particles* (Wiley-VCH, Weinheim, 2004).
- [99] M. I. Mishchenko, L. D. Travis, and A. A. Lacis, *Scattering, Absorption, and Emission of Light by Small Particles* (Cambridge University Press, Cambridge; New York, 2002).
- [100] A. Lagendijk, A. P. Mosk, and W. L. Vos, Mutual extinction and transparency of multiple incident light waves, *Europhys. Lett.* **130**, 34002 (2020).
- [101] A. Rates, A. Lagendijk, O. Akdemir, A. P. Mosk, and W. L. Vos, Observation of mutual extinction and transparency in light scattering, *Phys. Rev. A* **104**, 043515 (2021).
- [102] P. Hong and W. L. Vos, Controlled light scattering of a single nanoparticle by wave-front shaping, *Phys. Rev. A* **106**, 063502 (2022).
- [103] B. Semnani, J. Flannery, R. Al Maruf, and M. Bajcsy, Spin-preserving chiral photonic crystal mirror, *Light Sci. Appl.* **9**, 23 (2020).
- [104] V. Liu and S. Fan, S4 : A free electromagnetic solver for layered periodic structures, *Comput. Phys. Commun.* **183**, 2233 (2012).
- [105] R. Narayanaswamy and O. S. Wolfbeis, *Optical Sensors: Industrial Environmental and Diagnostic Applications* (Springer Berlin Heidelberg, Berlin, Heidelberg, 2004).
- [106] G. Cox, *Optical Imaging Techniques in Cell Biology*, 2nd ed. (CRC Press, Boca Raton, 2012).
- [107] G. Zheng, X. Cui, and C. Yang, Surface-wave-enabled dark-field aperture for background suppression during weak signal detection, *Proc. Natl. Acad. Sci. USA* **107**, 9043 (2010).
- [108] G. Zheng and C. Yang, Improving weak-signal identification via predetection background suppression by a pixel-level, surface-wave enabled dark-field aperture, *Opt. Lett.* **35**, 2636 (2010).
- [109] C. Guo, B. Zhao, and S. Fan, Adjoint Kirchhoff's law and general symmetry implications for all thermal emitters, *Phys. Rev. X* **12**, 021023 (2022).
- [110] T. Liu, C. Guo, W. Li, and S. Fan, Thermal photonics with broken symmetries, *eLight* **2**, 25 (2022).
- [111] L. W. Tu, *An Introduction to Manifolds*, 2nd ed. (Springer-Verlag, New York, 2011).
- [112] L. Dieci and A. Pugliese, Two-parameter SVD: Coalescing singular values and periodicity, *SIAM J. Matrix Anal. Appl.* **31**, 375 (2009).